

**Quasistatic kinetic avalanches and self-organized criticality in deviatorically loaded granular media**Jordi Baró <sup>1,2,\*</sup> Mehdi Pouragha <sup>3,4</sup> Richard Wan <sup>3</sup> and Jörn Davidsen <sup>1,5</sup><sup>1</sup>*Department of Physics and Astronomy, University of Calgary, 2500 University Drive NW Calgary, Alberta, Canada T2N 1N4*<sup>2</sup>*Centre for Mathematical Research, Campus de Bellaterra, Edifici C, 08193 Bellaterra, Barcelona, Spain*<sup>3</sup>*Civil Engineering Department, University of Calgary, 2500 University Drive NW Calgary, Alberta, Canada T2N 1N4*<sup>4</sup>*Department of Civil and Environmental Engineering, Carleton University, 1125 Colonel By Drive, Ottawa, Ontario, Canada K1S 5B6*<sup>5</sup>*Hotchkiss Brain Institute, University of Calgary, 3330 Hospital Drive NW, Calgary, Alberta, Canada T2N 4N1*

(Received 12 May 2021; accepted 8 July 2021; published 2 August 2021)

The behavior of granular media under quasistatic loading has recently been shown to attain a stable evolution state corresponding to a manifold in the space of micromechanical variables. This state is characterized by sudden transitions between metastable jammed states, involving the partial micromechanical rearrangement of the granular medium. Using numerical simulations of two-dimensional granular media under quasistatic biaxial compression, we show that the dynamics in the stable evolution state is characterized by scale-free avalanches well before the macromechanical stationary flow regime traditionally linked to a self-organized critical state. This, together with the nonuniqueness and the nonmonotony of macroscopic deformation curves, suggests that the statistical avalanche properties and the susceptibilities of the system cannot be reduced to a function of the macromechanical state. The associated scaling exponents are nonuniversal and depend on the interactions between particles. For stiffer particles (or samples at low confining pressure) we find distributions of avalanche properties compatible with the predictions of mean-field theory. The scaling exponents decrease below the mean-field values for softer interactions between particles. These lower exponents are consistent with observations for amorphous solids at their critical point. We specifically discuss the relationship between microscopic and macroscopic variables, including the relation between the external stress drop and the internal potential energy released during kinetic avalanches.

DOI: [10.1103/PhysRevE.104.024901](https://doi.org/10.1103/PhysRevE.104.024901)**I. INTRODUCTION**

Mechanical systems with evolving internal structure often exhibit intermittency or avalanche dynamics under quasistatic mechanical driving (see Refs. [1–3] for reviews). Specifically, intermittent athermal dynamics dominated by slip dislocations are observed in the plastic deformation of single crystals [4–6] as well as amorphous materials such as bulk metallic [7,8] and colloidal [9] glasses, high entropy alloys [10,11], and granular assemblies [12–14], with their prevalent dynamics being successfully captured through discrete element simulations in idealized athermal quasistatic (AQS) conditions considering Lennard-Jones (LJ) particles—simulating molecular dynamics in glassy materials [15–20]—as well as soft spheres [21,22]—simulating assemblies of larger spherical aggregates—and elastic interactions—simulating granular matter [23–25]. In granular materials, where potentials are exclusively repulsive, intermittency occurs upon the activation of *fragile* jammed states [26,27], where the system is consolidated in marginally stable solidlike configurations that become unstable under infinitesimal stress variations. Jamming states can only exist within certain conditions [27]. Under external mechanical driving, and in absence of thermal fluctuations, jamming is observed to be limited below

a macroscopic shear stress threshold,  $\sigma_c$ , often referred to as a critical point, which becomes stationary after an initial transient regime [28]. When the system is pushed above  $\sigma_c$ , jammed states are unlikely and the excess of free energy (corresponding to the excess of shear stress) is dissipated through particle rearrangements. Under *strain* driving, such dissipation reestablishes the mechanical stability at stress values below  $\sigma_c$ . Such a sequence of quasistatic metastable states leads to an elastoplastic stress-deformation response and the macromechanical state of the system eventually hovers around  $\sigma_c$ , which can be considered a case of *self-organized criticality* (SOC) [29–32] characterized by critical avalanche dynamics exhibiting scale-free behavior.

The hypothesis of SOC in the deformation of amorphous materials inspired the development of the theory of *elastoplasticity*, bridging the gap between macromechanical rheology models and SOC (see Ref. [3] for an extensive review). Elastoplastic models (EPMs), as defined in soft-matter physics [3], represent amorphous materials as lattices of bistable—either elastic or plastic—representative volume elements or sites. Under strain or stress driving, each site experiences an affine elastic deformation. When the local stress at a site overcomes a local threshold, representing a local mechanical instability, the element undergoes a local nonaffine plastic-deformation event involving a predefined stress propagator interacting with other elements and triggering an avalanche as a cascading event. Conceptual mean-field models interpret

\*jbaro@crm.cat

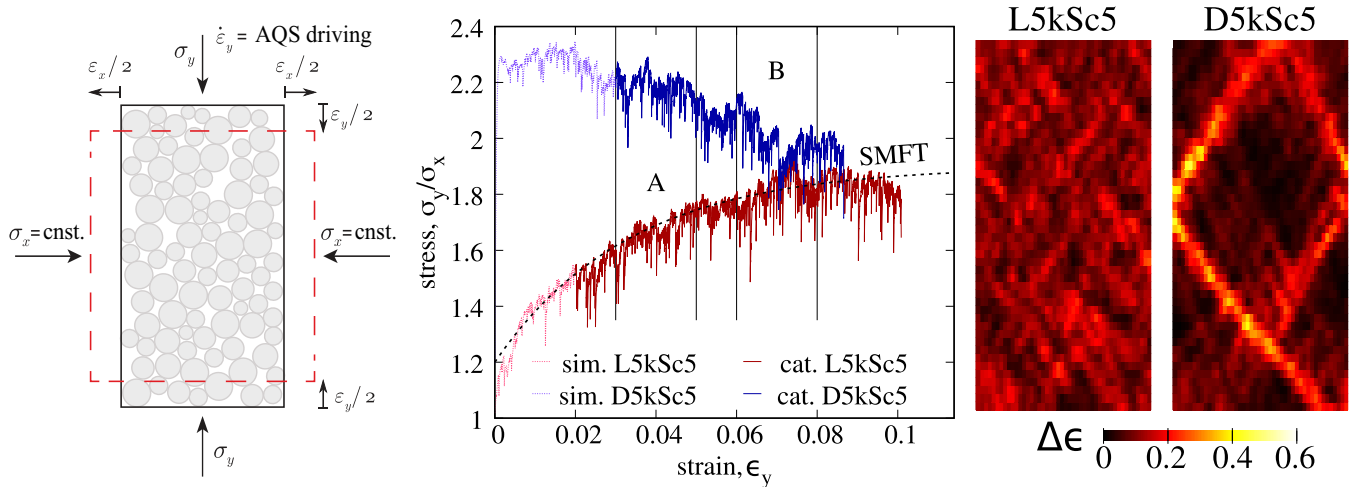


FIG. 1. Left: Schematic geometrical representation of the simulation. Center: Stress-strain response from simulation results (*sim.*) of samples D5kSc5 and L5kSc5. Avalanche catalogs (*cat.*) only consider the intervals represented in wider and darker lines. The black dotted line represents a fitted slip mean-field theory (SMFT) prediction (1) to L5kSc5. The statistical analysis represented in Fig. 5 corresponds to the subcatalogs constrained within strain intervals A and B of the evolution. Right figures represent the changes in deviatoric strain ( $\Delta\epsilon$ ) of both samples during the whole simulation, showing strong localization in D5kSc5.

the residual stresses to local instabilities as scalars undergoing a stochastic process [33]. Within this latter category, the simplified and mathematically solvable *slip mean-field theory* [12,34–36], considering all-to-all homogeneous site interactions, provides a remarkably apt conceptual model for a wide spectrum of processes including the macromechanics and the statistical features of externally measured avalanche dynamics in granular media [12,13,19,37–39]. Such results reinforced the idea of a predominant mean-field universality class in the avalanche statistics [3,12,13,18,19,39,40]. In the slip mean-field theory, SOC appears in the thermodynamic limit as an asymptotic approach to a regime at stress value  $\sigma_c$  characterized by a divergence of scales in avalanche statistics. Following scaling relations [36], the macromechanical evolutionary path of strain-driven ( $\epsilon$ ) amorphous solids leading to the steady-state flow regime is uniquely represented in the slip mean-field theory by the stress-strain relation:

$$\sigma(\epsilon) \approx \sigma_c [1 - \exp(-\epsilon)]. \quad (1)$$

Such a generalized macromechanical perspective is by construction insufficient to describe the dynamics and statistics of slip avalanches as a function of state [3]. Both experiments and discrete element simulations display a nonmonotonous evolution towards  $\sigma_c$ , implying that the relation  $\sigma(\epsilon)$  does not represent a function of state [22]. Furthermore, initial configurations determine the  $\sigma(\epsilon)$  response during such a transient regime and do not converge to  $\sigma_c$  through the same evolutionary path (e.g., Fig. 1). A widespread scientific endeavor aims to understand the limitations and discrepancies of atomistic discrete element models, coarse-grained full tensorial [25,41–43], scalar [30,44,45], and mean-field [33,45–48] EPMs under the lens of the micromechanics of avalanche dynamics [3,42,49]. Other studies focusing on the internal topology of the granular material suggest that the state of compact granular media is better parametrized by a micromechanical description of the particle configuration and the network of contact forces, which can be only partially represented in

terms of its macromechanics. Specifically, the role of internal structures to the mechanics of granular media has been discussed in early conceptual models [26,27], experiments [14,26,50–56], discrete element models [57–60], and new mechanical-statistical theories of granular matter [28,61–67]. Indeed, the definition of fragile matter is intrinsically linked to the existence of force-chain structures [26] and experiments reveal how the nucleation of failure events is directly linked to *local* topological measurements such as the betweenness centrality [56]. Parallel discrete element studies identified a *stable evolution state* (SES) in a space of independent structural variables. The SES is reached after an adaptation transient, reached considerably before the stationary flow regime observed in the macromechanical variables [24]. As an extended micromechanical representation of the jamming transition, the SES describes a subset of micromechanical states upon which the internal structure of granular media starts to evolve, leading to stick-slip-like events or avalanches. In particular, the same spontaneous shear localization leading to the non-monotonous macromechanical state evolution can degenerate into different evolutionary paths towards the flow regime even under similar initial conditions [68–71], reaching the same topological SES at different values of stress. The parametric study in Ref. [24] shows that once the SES is reached, regardless of the initial condition and material parameters, the granular assembly starts to exhibit irreversible deformations that are predominantly governed by microavalanches.

Here, we analyze the statistics of kinetic avalanches identified during AQS biaxial compression in discrete element simulations of granular assemblies. We interpret the results in the context of different hypotheses regarding the coarse-grained description of amorphous materials. We show how the distribution of avalanche sizes is independent of the macroscopic state of the system once the SES is reached, even when the macromechanical paths from different initial conditions (e.g., loose vs dense assemblies) differ significantly. More importantly, the SES itself exhibits the properties of a

self-organized critical state. Thus, while this critical state includes the final steady-state regime at the customary *critical* stress value  $\sigma_c$ , it is reached significantly earlier. Because of that, rather than using the unique term *critical point* to designate both, we will distinguish between the final *steady-state regime* at  $\sigma_c$  and *criticality* as the statistical mechanics concept referring to a divergence of susceptibilities. We also show that while the statistical avalanche behavior is stationary within the SES each individual avalanche modifies noticeably the state of the system, introducing a characteristic delay, also known as a *pseudogap*, in the interevent times between consecutive avalanches. This leads to stronger correlations between the states at which avalanches are triggered than between the states at which avalanches stop and suggests that the SES defines an evolving stability limit leading to the steady-state regime at the macroscopic scale rather than a stability basin towards which the system is relaxed after each avalanche. Moreover, we find nonuniversality in the power-law exponents defining the statistics of the energy transfers involved in avalanches. In this case, we expose a dependence of the exponents on the softness of the interactions between particles. The external stress drop is found to be approximately proportional to the drop of internal elastic energy caused by configurational changes, but, due to the presence of soft lateral walls, this is not the case for the energy dissipated by frictional forces and damping. The relation between internal energy drops and the peaks of kinetic energy is consistent with a specific set of assumptions within the slip mean-field theory. This consistency allows us to relate the nonuniversality of our results with a potential transition between the expectations of slip mean-field theory and elastoplasticity based on the estimated *critical exponents*.

The paper is organized as follows: In Sec. II we introduce our numerical discrete element simulations of granular assemblies, review the definition of the SES, and explain how the definition of kinetic avalanches is used to implement the quasistatic biaxial compression driving. In Sec. III we present the statistical analysis of the avalanche properties, focusing on the average relations between avalanche-size measurements, the existing correlations between events, and their full distributions with the corresponding fitted exponents. In Sec. IV we discuss the conditions and properties of avalanche criticality and compare them with the mean-field solution of elastoplastic models. Final conclusions are presented in Sec. V.

## II. BACKGROUND AND METHODS

### A. Computational model

The software package PFC2D [72] has been used here for discrete element simulation of two-dimensional (2D) granular assemblies under AQS compression. A linear contact model with constant stiffness is considered along normal and tangential directions with their respective stiffnesses,  $k_n$  and  $k_t$ , being the same and equal to  $10^9$  N/m. The tangential force is restricted by a Coulomb friction law  $f_t \leq \mu f_n$  with  $\mu = 0.5$  for all simulations. A numerical damping of 5% is also considered which acts as a draglike force on particles by artificially ramping changes in velocities (see Ref. [72] for exact definition). The radii of circles are uniformly distributed over  $r_{\min}$  and  $r_{\max}$

TABLE I. Simulation details for the nine numerical samples. The confining pressure is kept constant, and the driving rate is halted during the propagation of avalanches. The initial porosity is measured at the beginning of the simulation.

Name	No. of particles $N$	Confining pressure $\sigma_x$ (N/m)	Driving rate $\dot{\epsilon}_y$ ( $\times 10^{-9}$ s $^{-1}$ )	Initial porosity $\phi_0$
D20kSc5	19520	$10^5$	2.3	0.156
L20kSc5	19353	$10^5$	2.3	0.190
D5kSc5	6374	$10^5$	2.4	0.159
L5kSc5	5504	$10^5$	2.4	0.192
D2kSc5	1593	$10^5$	1.3	0.165
D5kSc6	6374	$10^6$	2.4	0.154
D5kFc5	6374	$10^5$	7.0	0.159
D5kFc6	6374	$10^6$	7.0	0.154
D5kFc7	6374	$10^7$	7.0	0.120

with  $r_{\max}/r_{\min} = 1.5$ , around an average radius of 1 mm. To avoid overcrowding the figures and for a better readability, the results in this paper are presented in their dimensional forms with SI units. The material and loading parameters adopted for numerical simulations are summarized in Table I.

The rectangular sample has an initial aspect ratio of 2 : 1 which is confined in between frictionless walls. During the initial so-called compaction stage, the particles are slowly inflated, as a common numerical technique, to obtain the target isotropic pressure on the walls. During this stage the interparticle friction is artificially modified to achieve the desired initial density. The friction is set to 0.5 at the end of compaction. Next, the deviatoric load is applied by moving the top and bottom walls towards each other with a straining rate of  $\dot{\epsilon}_y$  while the stress on the lateral walls,  $\sigma_x$ , is kept constant through a servo-control mechanism. The wall velocity is sufficiently small to keep the inertia number well below the quasistatic limit [73]. Moreover, to ensure a quasistatic loading, the driving is halted during surges in kinetic energy, as is explained in detail later. The typical stress-strain responses and internal displacement maps are exemplified by a pair of initially loose and dense assemblies in Fig. 1. A relatively monotonic and homogeneous average trend is seen for loose assembly (L5kSc5) while the dense assembly (D5kSc5) experiences a peak of stress before dropping to the steady-state regime at larger axial strains. This previous transient regime is linked to the formation of shear localization bands (see right-bottom map in Fig. 1)

### B. Internal dynamics

At any given instance, the energy of the granular system is composed of the following parts: The kinetic energy of particles,  $E_K$ ; the internal elastic energy stored at contact points,  $U$ ; the dissipation due to frictional and drag forces,  $D = D_f + D_d$ ; and the external work by vertical and lateral stresses,  $W_y$  and  $W_x$ , respectively. The balance of energies is given by  $W_y + W_x = U + D + E_K$ . For a system of  $N$  particles, the total instantaneous kinetic energy can be expressed as  $E_K(t) = \frac{1}{2} \sum_{i=1}^N (m_i v_i^2 + I_i \omega_i^2)$ , where  $m_i$  and  $I_i$  are the mass and moment of inertia of the  $i$ th particle, respectively, and  $v_i$  and  $\omega_i$  are translational and angular velocities. Considering

that the velocity of the lateral walls is, on average, proportional to the vertical driving rate, a characteristic value for total kinetic energy of a homogeneous sample can be defined as  $K_D := \frac{1}{6}N(m)(h\dot{\epsilon}_y)^2$ , where  $h$  is the sample's height. We use  $K_D$  as a reference parameter to define the energy thresholds for avalanche detection.

The microscopic configuration of contact points creates a heterogeneous landscape of elastic potentials. Even under monotonic driving the system exhibits a nonlinear mechanical response involving sharp local accelerations, complex internal velocity fields, and global bursts of internal kinetic energy that cannot be simplified in terms of the external measures such as  $\dot{\epsilon}_y^2$  [74]. Considering a quasistatically slow driving, the system is episodically trapped in a series of metastable jammed configurations well represented by the potential energy [75]. The external AQS driving pushes the system through local mechanical instabilities that trigger local dynamics in the form of frictional sliding between particles at contact points, or the collective buckling of chained contact forces [26,57,76]. These initial instabilities can develop into collective internal avalanches the propagation of which is almost independent of the driving speed and is controlled, instead, by particle-scale dissipative forces due to the draglike forces and interparticle friction.

**C. Stable evolution state**

The mechanical evolution of the assembly is determined by a sequence of episodes of quiescent deformation and sudden avalanches involving configurational rearrangements. Recent studies [24,60,71,77] suggested that mechanically stable configurations are constrained by the SES defined as a manifold observed in the space of three micromechanical variables: coordination number (average number of contacts per particle), rigidity ratio [average contact deformation relative to the particle size, which scales with  $(\sigma_x + \sigma_y)/k_n$ ], and fabric anisotropy (a measure for directional distribution of contacts), as represented in Fig. 2. The concept of the SES has been proven to be effective in developing new micromechanical constitutive models for granular materials [77].

Considering a dense sample, the initial state of the assembly is located on the stable side (right side in Fig. 2) of the SES. As the sample is loaded deviatorically, the microstructure quickly evolves through loss and gain of contacts approaching the SES limit [60]. Upon reaching the SES, the assembly appears to have just enough constraints to retain metastable static equilibrium [24,75]. Based on its close connection to jamming transition and isostaticity [24], the SES manifold divides the space of microscopic states into two zones: (1) the statically stable, jammed zone where higher coordination numbers prevent plastic structural evolutions, and (2) the unjammed zone where the structure can freely evolve, but static equilibrium cannot be attained due to low coordination number. Considering that a quasistatic regime requires both evolution of microstructure and static equilibrium, it is natural that such a regime occurs only near the SES manifold for any initial configuration. At the SES, the additional deviatoric straining introduced by the monotonic driving acts as an initial perturbation pushing the assembly beyond the stability limit and triggering the avalanche as

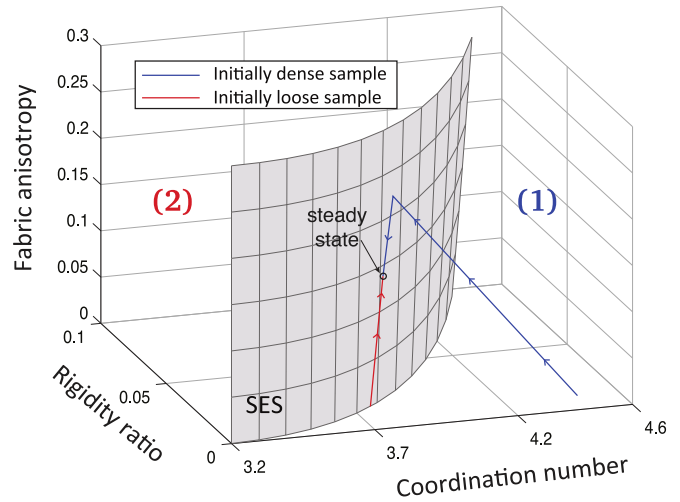


FIG. 2. Schematic visualization of the SES surface and the material state path for initially loose and dense samples. The response of the dense sample (blue) starts at the jammed half space (1) outside of the SES but rapidly approaches the surface and remains on it afterwards. The micromechanical state of the loose sample (red) is situated on the SES surface all along the deviatoric loading history. All configurations in the unjammed half space (2) are mechanically unstable. The metastable, stick-slip-like response in stress is observed only when the micromechanical state of granular assembly reaches the SES.

a sudden increase in the internal kinetic energy. Kinematic momentum is known to modulate the jamming transition in shear processes [23,78–80] and alters the stability conditions during the transition. The kinematic momentum caused by avalanches is rapidly dissipated, hence acting as a transient overshooting mechanism [81] pushing the system away from the fragile SES towards more stable (nonfragile) configurations under quasistatic conditions, as discussed in more detail later in Sec. III D.

The resulting sequence of avalanches involves rearrangements adjusting the number and orientation of contacts bringing gradually the micromechanical state of the granular assembly towards the steady state at  $\sigma_c$ , where the deviatoric straining is sustained with no appreciable change in the micromechanical state of the assembly. The evolution within the SES towards the final steady state is not necessarily unique and depends on the original configuration and loading path. This is most clearly observed for the initially loose cases the initial state of which falls on the SES (see Fig. 2).

**D. Quasistatic driving and kinetic avalanches**

To guarantee a quasistatic condition and, in particular, a clean separation between independent avalanches, in our simulations, the driving is halted as soon as an avalanche is detected. Such a detection occurs when the total kinetic energy  $[E_K(t)]$  exceeds a selected threshold value  $K_h = 3K_D$ . A similar strategy was used by Refs. [16,17] for the discrete element simulations of amorphous materials. As an example, Fig. 3 shows the assembly magnitudes in a typical simulation (D5kFc6) during the time interval containing two avalanches. The jumps in  $E_K(t)$ , up to several decades [Fig. 3(a)], signal

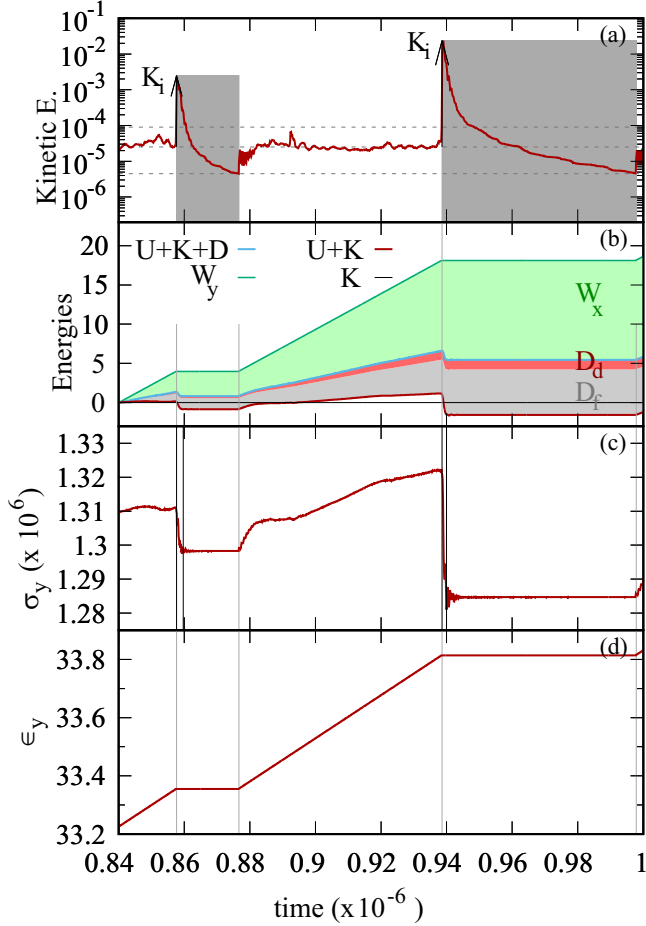


FIG. 3. Close-up example (D5kFc6) of the macromechanical evolution of the system during the span of two consecutive avalanches as a function of time. (a) Evolution of the total kinetic energy  $[E_K(t)]$  used to define the avalanches and the driving protocol, which halts the driving above  $K_h$  (upper dashed line) and restarts it when  $E_K(t) > K_r$  (lower dashed line). The middle dashed line indicates the expected average kinetic energy during driving. The intervals of the avalanche relaxation time without driving are indicated by the gray area. (b) Energy transfer during driving and avalanche propagation. The supplied work ( $W_y$ ) is represented as a green line. The green area represents the part of the work invested in lateral expansion of the system against the confining pressure ( $W_x$ ). The blue line represents the rest of the work transformed into heat (dissipation  $D$  and transient kinetic energy  $E_K$ ) and the final variation of the internal energy ( $U$ ). Energy is dissipated by a medium draglike force ( $D_d$ ) and friction between particles ( $D_f$ ) represented as red and gray areas respectively. (c) Avalanches are always accompanied by a drop in the internal energy that matches a drop in the external vertical stress ( $\sigma_y$ ). We use the derivative of this stress drop to measure the duration of the avalanche. (d) The driving stops during the relaxation time of the avalanche. The relation between  $\sigma_y$  (c) and  $\epsilon_y$  (d) is represented in Fig. 1 for two other simulations.

the onset of avalanches triggered by the sudden release of elastic potential energy [Fig. 3(b)]. Such a release of elastic energy is signified also by the drop in the boundary stress,  $\sigma_y$  [Fig. 3(c)], while the lateral strain is adjusted to keep  $\sigma_x$  constant. The surplus of kinetic energy is dissipated over

time by frictional sliding and draglike forces [Figs. 3(a) and 3(b)]. Since the simulations are athermal, the heat transfer due to dissipation compensates the loss in internal energy. The numerical results exhibit dissipation intervals [gray areas in Fig. 3(a)] considerably longer than the duration  $T$  of the first rebound ( $\dot{U} \geq 0$ ) of the potential energy release [Fig. 3(c)]. Once  $E_K(t)$  is damped below  $K_r = 0.15K_D$ , the external driving is resumed. The factors defining  $K_h$  and  $K_r$  from the base  $K_D$  have been selected to optimize the resolution and the computational speed. The values of  $K_h$  are just above noise fluctuations in all of our simulations, and  $K_r$  is low enough to represent a precise measure of the dissipated energy guaranteeing the quasistatic limit.

We obtain an avalanche catalog by labeling individual avalanches with a sorted index  $i$  and represent them as a marked point process. Instead of the instant in simulation time  $t_0$  when the  $i$ th avalanche initiates at  $E_K(t) \geq K_h$ , we select  $\epsilon_y(t_0)$  as our temporal scale, which is stationary during the propagation of the avalanche because of the quasistatic driving. We also record the “size” of each avalanche as measured by different means. In particular, we focus in this paper on the duration  $T$  of the potential energy release  $\Delta U := U(t_0) - U(t_0 + T)$ ; the stress drop  $\Delta\sigma_y := \sigma_y(t_0) - \sigma_y(t_0 + T)$ ; the peak in kinetic energy  $K = E_K^{\max} - K_D$ ; the total dissipated energy until the quasistatic driving resumes,  $D = D_f + D_d$ , which accounts for the friction at the contact points ( $D_f$ ) and the draglike forces ( $D_d$ ); and the work against the lateral walls  $W_x = \int_{t_0}^{t_0+T} V(t)\sigma_x\dot{\epsilon}_x dt$ , where  $V(t) := V_0\epsilon_x(t)\epsilon_y(t) = V_0(1 + \epsilon_v)$  is the 2D volume of the assembly the variation of which during a given avalanche can be safely neglected. The term *kinetic avalanches* is used here to specify the avalanche detection method and driving protocol, based on the internal kinetic energy. However, following the observations presented below, we will argue that most avalanche detection protocols based on other physical measures such as external stress or internal elastic energy drop would render similar results.

In the following sections, we study avalanches occurring within the SES, including avalanches before reaching the steady state (see intervals A in Fig. 1). The behavioral characteristics of all assemblies at the SES are argued to be the same [24]. We will verify that avalanche statistics are stationary within the SES regime from the analysis of subcatalogs, such as the intervals A and B represented in Fig. 1.

### III. RESULTS

#### A. Energy partition and avalanche scaling relations

As illustrated for the interval represented in Fig. 3(b), the energy supplied to the system as external work along the  $y$  axis  $[W_y = \int V\sigma_y d\epsilon_y = \int V_0(1 + \epsilon_v)\sigma_y d\epsilon_y]$  is mostly dissipated during the avalanche processes ( $D$ ) or transferred to the lateral walls ( $W_x$ ). The difference corresponds to variations in the elastic potential energy  $\Delta U$ . Instead of following a random sequence of drops and loads,  $U$  self-organizes towards a stationary value—determined by the flow regime in terms of elastoplasticity, or the SES in terms of granular microstructure—and fluctuates around that value through a sequence of loading and avalanche cycles.

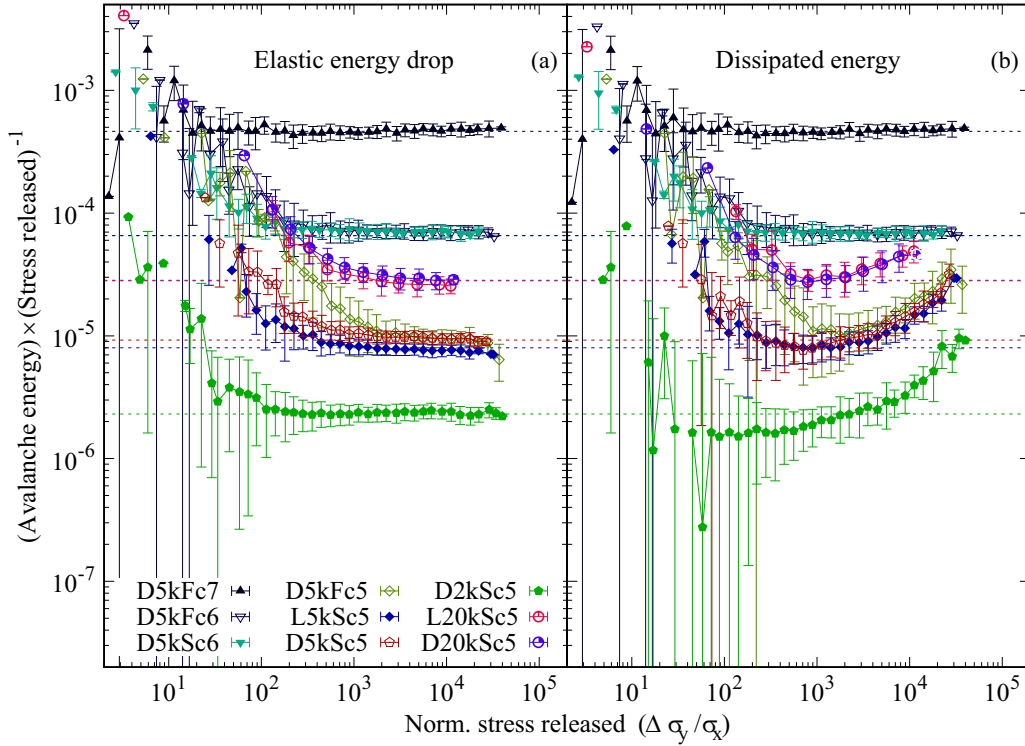


FIG. 4. Relation between normalized stress released ( $\Delta\sigma_y/\sigma_x$ ) and (a) average elastic potential released [ $\langle\Delta U\rangle(\Delta\sigma_y)$ ] or (b) dissipated energy [ $\langle D\rangle(\Delta\sigma_y)$ ] for stress released. Error bars correspond to one standard deviation. Dashed lines represent an asymptotic relation between the energy magnitudes and  $N\sigma_x^{0.85}$  which fits the results as discussed in Sec. III A.

This metastable cascade appears also in the external macromechanics of the assembly, i.e., in the stress drop ( $\Delta\sigma_y$ ). For kinetic avalanches, Fig. 4 tests the linearity between the external  $\Delta\sigma_y$  and the internal elastic potential drop averaged at  $\Delta\sigma_y$  windows,  $\langle\Delta U\rangle(\Delta\sigma_y)$  (left), as well as the average dissipated energy,  $\langle D\rangle(\Delta\sigma_y)$  (right). Recalling that the lateral stress is kept constant,  $\sigma_x$  is considered as the characteristic stress measure and, as such, the normalized stress release ( $\Delta\sigma_y/\sigma_x$ ) is used for describing the avalanche size. On average, and for sufficiently large avalanches,  $\Delta U$  is approximately proportional to  $\Delta\sigma_y$  in all simulations. This is different from the behavior of  $\langle D\rangle$ : For most simulations,  $\langle D\rangle$  is not proportional to  $\Delta\sigma_y$ , though such a proportionality has been observed in other works [16]. The difference between  $\langle D\rangle(\Delta\sigma_y)$  and  $\langle\Delta U\rangle(\Delta\sigma_y)$  reflects the contribution of the lateral walls to the energy balance ( $W_x$ ), which appears to be more prominent for large avalanches but disappears at high confining pressures. In addition, we observe a scaling factor, matching an apparent relation  $\Delta U \propto N\sigma_x^{1.85(5)}\Delta\sigma_y/\sigma_x$ . This relation is represented as horizontal dashed lines in Fig. 4. This scaling relation is reasonably close to the expectations from a dimensional analysis as detailed in Appendix A.

### B. Distribution of avalanche sizes

In addition to the scaling relations between different measures of avalanche sizes, the distribution of these sizes close to criticality also satisfies scaling relations of interest for the comparison with other avalanche phenomena and modeling approaches (see Sec. IV). Figure 5 shows the binned

avalanche distributions for  $K$  and  $\Delta U$  on a log-log scale for a loose and a dense assembly of  $N \sim 5000$  particles under similar external and internal conditions during different time intervals. In particular, the external stress in the assemblies is considerably different during interval A, and evolves towards almost indistinguishable stress values (B) as both systems approach the steady-state regime (see Fig. 1). Note that in a

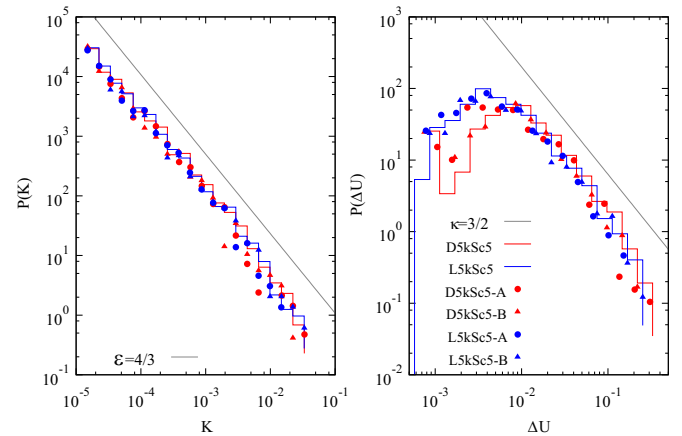


FIG. 5. Distributions of (a) kinetic energy peaks ( $K$ ) and (b) internal energy drops ( $\Delta U$ ), for L5kSc5 and D5kSc5 separated into stages A and B (see Fig. 1) compared with the total sequences in the SES regime. Exponent values [ $P(K) \sim K^{-4/3}$  and  $P(\Delta U) \sim \Delta U^{-3/2}$ ] expected from slip mean-field theory are shown for comparison (black lines).

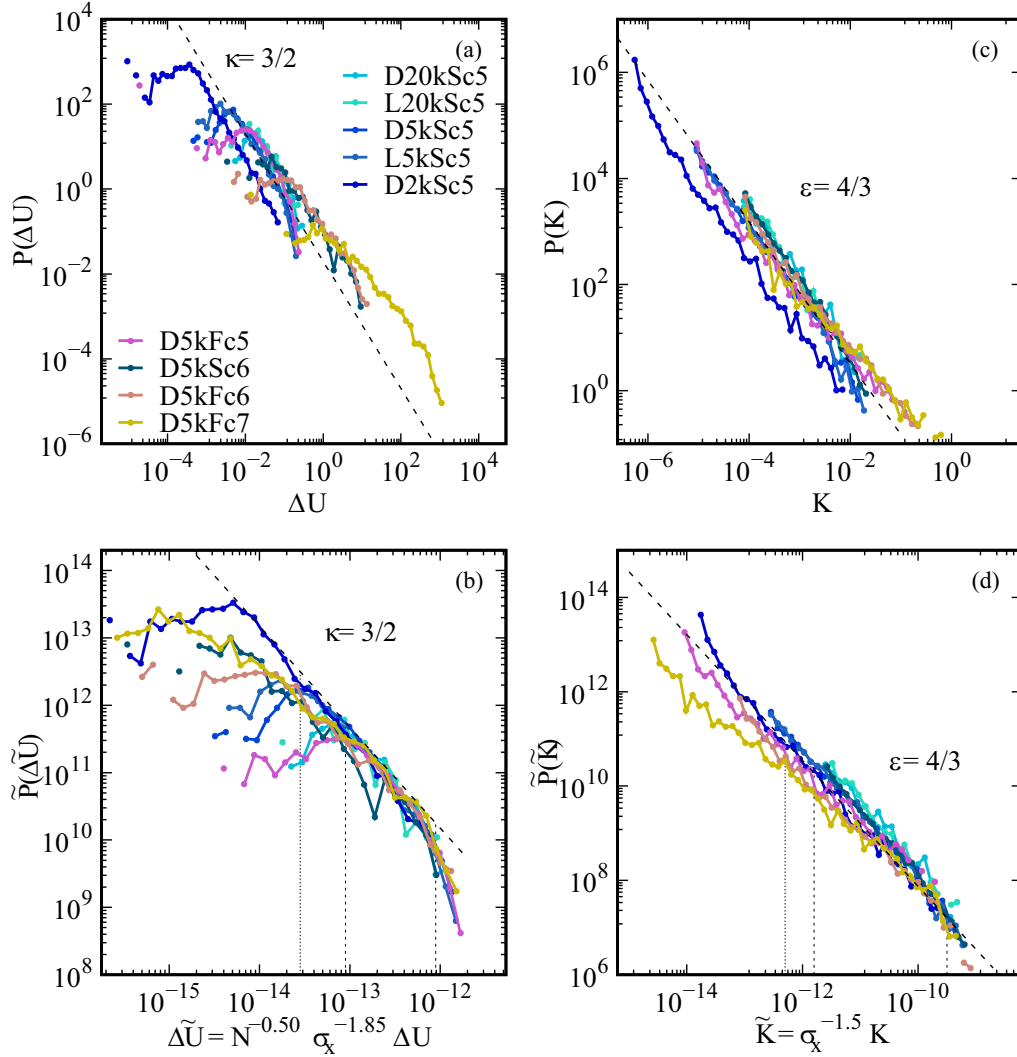


FIG. 6. Distributions of (a, b) internal energy drops ( $\Delta U$ ) and (c, d) kinetic energy peaks ( $K$ ) for all simulations. All distributions are shown on a regular scale (a, c) and rescaled to fit the apparent scaling relations in the  $x$  axes (b, d). The  $y$  axes are scaled to collapse the distributions to a single curve in the region of large values. Vertical dashed lines denote the intervals used to estimate the power-law exponents (dotted lines correspond to the lower limit for  $\sigma_x \geq 10^6$ ).

macromechanical formulation, the state of the material is different during strain hardening (interval  $A$  for the loose case), strain softening (interval  $A$  for the dense case), and close to the steady state (interval  $B$ ). However, despite such differences in stress state and the softening or hardening rate, no pronounced differences between the distributions are present in Fig. 5. Both distributions of  $\Delta U$  and  $K$  appear to be compatible with the scale-free hypothesis, i.e., the distributions follow a power-law decay,  $P(\Delta U) \sim \Delta U^{-\kappa}$  and  $P(K) \sim K^{-\varepsilon}$ , to a good approximation over a wide range of scales, although finite-size effects and limited statistics might play a role. By construction, avalanches are limited to  $K > K_h - K_D$ , rendering a sharp cutoff in  $P(K)$  for low values. Due to the average scaling relation between the values of  $K$  and  $\Delta U$  (Fig. 7) this cutoff appears as a smoother cutoff for low values in the distribution  $P(\Delta U)$ . The collapse of data with different initial densities and stress values further confirms that the state of the material associated with metastable avalanches is not sufficiently represented by macromechanical state vari-

ables, such as stress ratio and porosity, as commonly used in coarse-grained models. Considering that avalanche statistics can be represented in terms of state variables one needs a higher-dimensional space capable of representing all states with coinciding statistical properties, such as intervals  $A$  and  $B$  of dense and loose assemblies, in a unique manifold. In this regard, here we propose the SES as a viable candidate for such representation, since all evaluated intervals fall inside the SES manifold.

To further investigate the collapse of the avalanche data, we focus on the standard scaling ansatz for self-similar behavior:

$$P(x)dx = x^{-\tau_x} \Phi_x(x/x^*)dx, \quad (2)$$

where  $x$  is a measure of the avalanche size,  $\tau_x$  is the associated critical exponent,  $\Phi_x$  is a universal scaling function, and  $x^*$  is a characteristic avalanche size. This characteristic  $x^*$  should be controlled by the finite system size as well as by other parameters. We attempt the following general ansatz motivated by the usual relations found in finite-size scaling of scale-free

phenomena [82]:

$$x^*(N, \sigma_x, \dot{\epsilon}_y) = \tilde{x}^* N^{\gamma_N^x} \sigma_x^{\gamma_\sigma^x} \dot{\epsilon}_y^{\gamma_{\dot{\epsilon}}^x}. \quad (3)$$

If the scale-free hypothesis is valid,  $\Phi_x$  should be universal and all the distributions of  $x$  obtained with different parameters should collapse when rescaled by the characteristic event size, i.e., the distribution of  $\tilde{x} := x/x^*$  should be independent of system size and parameters. Figure 6 shows the distribution of  $\Delta U$  (a, b) and  $K$  (c, d) without scaling (a, c) and scaled (b, d) according to Eq. (3) using the best exponents found to collapse the exponential cutoffs into a single curve on visual inspection. Note that the y axes are normalized independently, since the normalization of the distributions is nontrivially affected by the lower cutoffs. We find a reasonable collapse for  $\gamma_\sigma^{\Delta U} = 1.85$  for potential energy drops and  $\gamma_N^{\Delta U} = 0.50$  corresponding to a fractal dimension  $d_f^{\Delta U} := d \times \gamma_N^{\Delta U} = 1$ , where  $d$  corresponds to the dimension of the specific system, which is 2 for our model. The dependence on  $\sigma_x$  is reasonable from the analysis in Sec. III A, if we assume that the intrinsic measure  $\Delta\sigma_y/\sigma_x$  is also characteristic of the avalanche propagation at a given simulation size [21]. For the peaks of kinetic energy ( $K$ ) we find a good agreement with  $\gamma_\sigma^K = 1.5$ , and  $\gamma_N^K = 0.0$ . Therefore,  $K$  appears to be an intensive quantity. We argue that the instantaneous  $E_k$  is probably dominated by a few fast-moving particles at a size-independent characteristic speed. In agreement with the quasistatic hypothesis, we do not observe any apparent relation with the speed of the external driving ( $\dot{\epsilon}_y$ ), such that  $\gamma_{\dot{\epsilon}}^x = 0$ , except for a shortening of the scale-free regime. The latter is caused by the lower bound of the power-law behavior controlled by the applied threshold  $K_h$  in the definition of the avalanches, which results in a sharp cutoff in  $K$  which in turn translates into a smoother transition in  $\Delta U$  leading to the decreased exponent and smoother lower cutoff in the distributions. The distribution of avalanche durations is presented in Fig. S1 of the Supplemental Material [83]. Such distributions appear to be compatible with a power-law distribution  $P(T) \sim T^{-\alpha}$  with exponent  $\alpha \approx 2$ . Yet, the power-law range is too short to provide a reliable estimate of the exponent.

The bivariate distribution of  $\Delta U$  and  $K$  of individual avalanches agrees with the scaling relation found in Fig. 6. In particular, Fig. 7 shows the average duration  $\langle T | \Delta U \rangle$  (a) and the rescaled kinetic peaks  $\langle \tilde{K} | \Delta U \rangle$  (b) expressed in bins of  $\Delta U$ . Over a range of a factor 25 in  $\Delta U$  ( $x$  axis in Fig. 7) and 150 in  $K$  [y axis in Fig. 7(b)], the conditional averages for all simulations collapse and agree with a power-law relation between avalanche energies:  $\langle \tilde{K} | \Delta U \rangle \propto \Delta U^\gamma$  with  $\gamma = 1.71(9)$ . As a particular case, a clear lower exponent is found at high confining pressures (D5kFc7). In a similar way, we can assess the average relation between  $\Delta U$  and the duration of the avalanche  $T$ , rendering a power-law relation  $\langle T | \Delta U \rangle \propto \Delta U^{0.20(3)}$ . Notice that the values of  $T$  have not been scaled since no clear parameter nor size dependencies have been observed in its distribution.

Visually, the exponent values seem to be in reasonable agreement with the expected values of the slip mean-field theory:  $\varepsilon = 4/3$ ;  $\kappa = 3/2$ , represented as dashed lines in Fig. 6; and  $\gamma = 3/2$  (see Sec. IV for an extended discussion). However, a closer inspection reveals a clear dependency on confining pressure. In order to estimate their actual values we

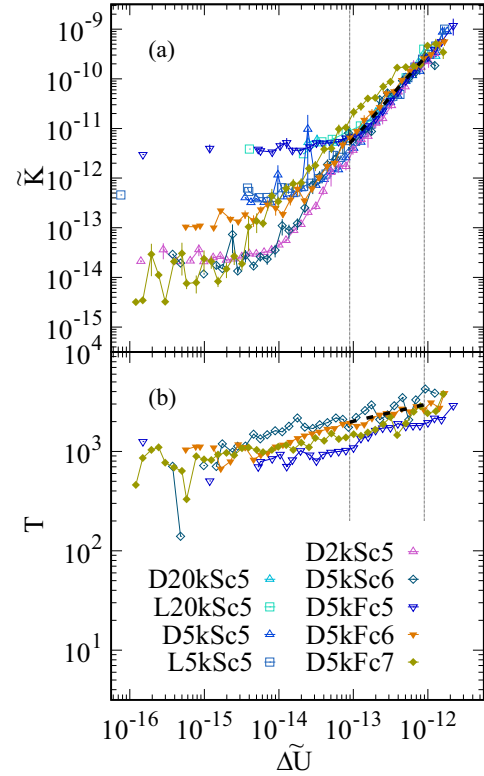


FIG. 7. Average relations between the potential energy drop ( $\Delta U$ ), kinetic peak ( $\tilde{K}$ ), and duration of the energy drop ( $T$ ). Units have been rescaled according to the exponents represented in Figs. 6(b) and 6(d); see main text for details. Black dashed lines: Fitted power law ( $\langle \tilde{K} | \Delta U \rangle$ ) for all simulations. Averages scale to a single relation with exponents close to an average  $\gamma = 1.71(9)$ . (a) Mean kinetic peak ( $\langle \tilde{K} | \Delta U \rangle$ ) for all simulations. Averages scale to a single relation with exponents close to an average  $\gamma = 1.71(9)$ . (b) Mean duration ( $\langle T | \Delta U \rangle$ ) for simulations D5kFc5, D5kSc6, D5kFc6, and D5kFc7; averages scale as  $\langle T | \Delta U \rangle \sim \Delta U^{0.177(9)}$ .

evaluate the avalanche sizes in their rescaled form considering the exponents used in Fig. 6 and the ranges of scale invariance shown as black segments in Fig. 7, to mitigate the effect of  $K_h$  on  $\Phi_x$ .

The exponents  $\kappa$  and  $\varepsilon$  characterizing the distributions of  $\Delta U$  and  $K$ , respectively, have been estimated using the maximum likelihood method following the recipe in Ref. [86] and summarized in Appendix B. All estimated exponents are summarized in Table II and represented in Fig. 8 as a function of the confining pressure  $\sigma_x$ . Table II includes the least square fit of  $\gamma$  for each experiment and Fig. 8 represents as well the expected exponents considering the approximated scaling relation  $\tilde{K}(\Delta U) \approx \langle \tilde{K} | \Delta U \rangle \propto \Delta U^\gamma$ , which renders the scaling relation between exponents:

$$\gamma = \frac{1 - \kappa}{1 - \varepsilon}. \quad (4)$$

This relation can be deduced from Eq. (2). The maximum likelihood estimation method reveals that both exponents  $\hat{\kappa}$  and  $\hat{\varepsilon}$  decrease with the confining pressure, from  $\hat{\kappa} = 1.58(11)$  and  $\hat{\varepsilon} = 1.36(4)$  for  $\sigma_x = 10^5$  to  $\hat{\kappa} = 1.14(6)$  and  $\hat{\varepsilon} = 1.02(8)$  for  $\sigma_x = 10^7$ . The exponent  $\hat{\gamma}$  also decreases from 1.82(10), close to the value 1.71(9) found by averaging all the conditional average dependencies of Fig. 7, to the value 1.48(7) for

TABLE II. Summary of the number of kinetic avalanches and critical exponents estimated from the simulations. Errors in brackets represent the standard deviation estimate from the likelihood function given a Gaussian approximation. For comparison, the predictions of slip mean-field theory considering  $K = E$  (SMFT<sup>(1)</sup>) and  $K = E_m$  (SMFT<sup>(2)</sup>) [36] (see Sec. IV) are also shown together with published findings of 2D full tensorial finite element simulations [42] and EPM simulations [3]. Note that similar exponents are also found in some discrete element simulations of shear processes [84,85] while other discrete element simulations return values as low as  $\kappa = 0.98(1)$  [20].

	Stiffness	No. events	$\kappa$	$\varepsilon$	$\gamma$
D2kSc5	(stiff limit)	1684	1.62(10)	1.32(10)	1.95(5)
L5kSc5	(stiff limit)	979	1.60(7)	1.34(5)	1.85(10)
D5kSc5	(stiff limit)	788	1.71(8)	1.33(6)	1.83(4)
L20kSc5	(stiff limit)	130	1.77(17)	1.45(6)	1.85(15)
D20kSc5	(stiff limit)	236	1.49(11)	1.36(4)	1.69(6)
D5kFc5	(stiff limit)	1215	1.46(6)	1.36(4)	1.71(5)
D5kSc6		396	1.41(8)	1.14(11)	1.65(8)
D5kFc6		851	1.32(5)	1.14(6)	1.71(4)
D5kFc7	(soft limit)	633	1.08(3)	1.02(8)	1.48(7)
SMFT <sup>(1)</sup>			1.5	$1 + \frac{\kappa-1}{2-\zeta\nu z} = 1.33$	$2 - \zeta\nu z = 1.5$
SMFT <sup>(2)</sup>			1.5	$(\mu + 1)/2 = 1.5$	$2\zeta\rho = 1$
2D EPM			1.25–1.28	$\approx 1.2$ [42]	$\approx 1.45$ [42]

$\sigma_x = 10^7$  (golden lines in Fig. 7). In general, the maximum likelihood method provides a more robust estimation of the exponent  $\varepsilon$  than  $\kappa$ . This is probably a consequence of the extended scale-free regime in  $K$ , given the lower exponent values and the sharper cutoff at  $K_h$ . The scaling relation captured by Eq. (4) is consistent with the estimated exponents when used to determine  $\kappa(\hat{\varepsilon}, \hat{\gamma})$  and  $\varepsilon(\hat{\kappa}, \hat{\gamma})$ , especially at low confining pressures. The consistency between the two estimation methods asserts the robustness of the results and the existence of an actual dependence beyond statistical artifacts that could alter the exponent estimation within the fitting intervals. We notice as well that this agreement survives at

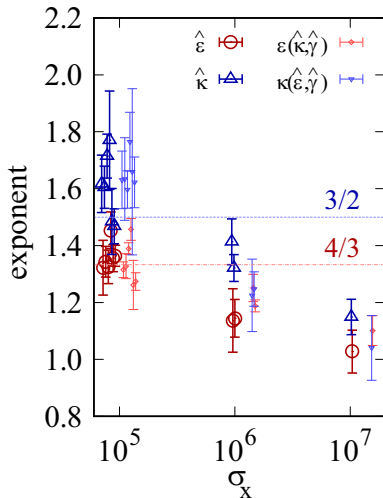


FIG. 8. Estimated exponents  $\kappa$  (blue triangles) and  $\varepsilon$  (red circles) as a function of the confining pressure within the intervals represented in Figs. 6 and 7. Error bars represent one standard deviation of the normal approximation to the likelihood function. Smaller points represent the estimation of each of the exponents with the help of Eq. (4) by using the other exponent and the estimated  $\hat{\gamma}$  (see Table II) to check the consistency of the results. Dashed lines represent the expected values of  $\kappa$  (blue) and  $\varepsilon$  (red) from slip mean-field theory.

high confining pressures, close to the singular undetermined point at  $\varepsilon \approx \kappa \approx 1$ . Such values are close to the values reported in discrete element simulations with LJ potentials [20]. Note that lower scaling exponents ( $\tau_x < 1$ ) are not expected in the framework of scale invariance since they would imply a divergence of energy released for large system sizes. However, it is possible that *estimated* exponents ( $\hat{\tau}_x$ ) in *finite* systems are lower even though the true scaling exponent is  $\tau_x = 1$ . This difference corresponds, in that case, to the form of the scaling function  $\Phi_x(x/x^*)$  [87]. Variations of exponents as a function of input parameters or conditions are fairly common in discrete element [17,88] and finite element [42] simulations of amorphous materials exhibiting SOC, but they are seldom observed in conceptual models and they are usually linked to the superposition of different subcritical processes [89,90], the sweeping through criticality [91], or rare regions, also known as *Griffiths phases* [92].

### C. Temporal correlations

Considering the selected AQS driving protocol, the time between avalanches is best defined in terms of the strain component  $\epsilon_y$ , since  $\dot{\epsilon}_y$  is constant during external driving and zero during the avalanche propagation intervals, i.e., avalanches are instantaneous in terms of  $\epsilon_y$ . Thus, interevent times are represented as  $\Delta\epsilon_y$ . Correlations between avalanches are often observed in natural mechanical processes. In particular, we are interested in the presence of temporal clustering, linked to triggering phenomena, which is often observed in natural systems [93–101] but seldom reproduced in conceptual constitutive models unless explicitly introduced [38,102–108]. Conversely, conceptual and numerical elastoplastic models identify a power-law relation in the distribution of the local residual stresses or stability limits close to the steady state, also known as the *pseudogap* [22,33,41,45,46] leading to quasiperiodicity in the strain increments between consecutive avalanches [47]. Recent studies revealed that the pseudogap is more prominent for large system sizes [43,48,109], contrasting with the naive expectation of quasiperiodicity being

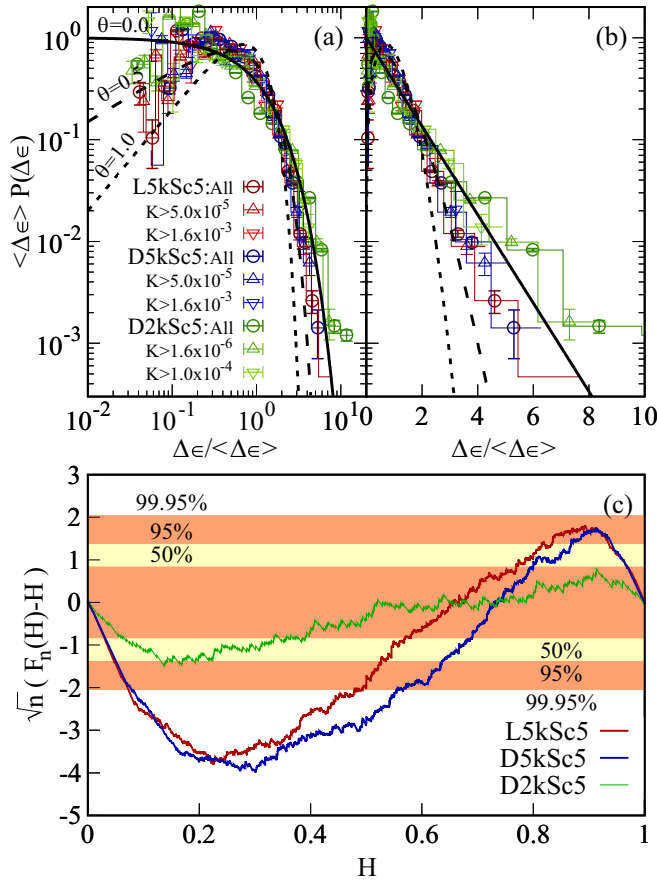


FIG. 9. (a, b) Distribution of interevent times as measured by the strain difference  $\Delta\epsilon_y$  for different  $K$  thresholds (corresponding to 100,  $\approx 50$ , and  $\approx 10\%$  of the events) and scaled by average  $\langle \Delta\epsilon_y \rangle(K)$  in (a) log-log and (b) linear-log scales, exemplified by three different simulations. For comparison, we show the Weibull renewal model (black lines) predicted by EPM [see Eq. (7)] with  $\theta = 1.0, 0.5$ , and  $0.0$ , the latter corresponding to a homogeneous Poisson process. (c) Kolmogorov-Smirnov test over the  $H$  values obtained by the Bi test for Poisson rejection (see text) where  $n$  is the number of interevent times. Color bands represent confidence intervals for rejection as indicated in the labels.

caused solely by finite-size effects. We address this question in Sec. IV B through the analysis of  $\Delta\epsilon_y$  presented here.

Figure 9 shows the statistical analysis of the time between avalanches as measured by the axial strain increment  $\Delta\epsilon_y$  for selected samples L5kSc5, D5kSc5, and D2kSc5 used here as examples. Each of the lines represent the strain increments between consecutive events with energy  $K$  above different thresholds values. The distribution of interevent times in linear-log scale [Fig. 9(b)] follows an exponential distribution for long interevent times, suggesting that avalanches are independent of one another and follow a Poisson process with a stationary characteristic avalanche rate [97,110,111]. Similar results have been recently reported by Kuhn and Daouadji [112] for nonspherical particles. In contrast, self-excitations usually involve strong correlations between large events [93,97] which would be easily identified as an excess of short interevent times. No such excess is observed in Fig. 9(a). Therefore we can rule out the presence of self-excitations in

our simulations. In contrast, most threshold values reveal a deficit of short interevent times compared to a homogeneous Poisson process in all simulations. This implies regularity, i.e., the existence of characteristic (quasiperiodic) interevent times, which might be linked to finite-size effects or the aforementioned pseudogap.

This deviation from Poisson behavior in the avalanche process can also be verified by the rejection method first proposed in Ref. [113], the so-called Bi test, detailed in Appendix C. The Kolmogorov-Smirnov test over the  $H_i$  values shown in Fig. 9(c) displays a rotated “S” profile characteristic of regular processes, in opposition to a rotated “Z” profile, which is associated with clustering or self-excitation mechanisms [99]. The S profile is clear in all simulations (see the profiles represented in Fig. S2 of the Supplemental Material [83]). The Poisson hypothesis is rejected at 95% confidence interval in all simulations and at 99.95% in most of them, including D5kSc5 and L5kSc5. In the case of D2kSc5 the  $F_n(H)$  distribution falls short to reject the Poisson hypothesis at the 99.95% confidence interval. This discrepancy is in line with the better agreement with a Poisson process observed for the distribution of waiting times of D2kSc5 (Fig. 9). We verified numerically that the deficit of short interevent times is more pronounced in larger simulations. In particular, the fraction of rescaled interevent times below the expected first quartile of a normalized exponential distribution is  $\approx 0.2$  for  $\approx 2000$  particles,  $\approx 0.13$  for  $\approx 5000$  particles, and  $\approx 0.08$  for  $\approx 20000$  particles with respect to the expected  $0.25$  if the process were Poissonian (see Fig. S5 in the Supplemental Material [83] representing the fraction of events below the expected first quartile under the Poisson hypothesis). Unfortunately, since the threshold selection to define avalanches is size dependent, we cannot straightforwardly infer the relation  $\langle \delta(N) \rangle$  which is expected to go as  $N^{d/d_f - 1}$  [21].

#### D. Stress correlations

Figure 1 shows that the macromechanical state of the system is constrained within an evolving narrow stripe following a well-defined path at the large scale. However, the commonly used smooth average stress-strain relation is clearly a broad approximation. At the scale displayed in Fig. 3 the intrinsic metastable dynamics arising from the competition between the slow driving and the fast relaxation in the form of avalanches exhibits its nonsmooth behavior. As an example, Fig. 10(a) shows a close-up to the macromechanics of one of the simulations. We mark the stress ( $\sigma_y$ ) at the onset of the avalanche [ $\sigma_y(t^-)$ ] and at the end of the avalanche [ $\sigma_y(t^+)$ ]. Figure 10(a) also shows an example of interevent loading time  $\Delta\epsilon_y^k = \epsilon_{y,k+1} - \epsilon_{y,k}$ , preceded by an avalanche  $k$  with stress drop  $\Delta\sigma_{y,k}$  and followed by an avalanche  $k+1$  with stress drop  $\Delta\sigma_{y,k+1}$ . The regularity in the distribution of interevent times exposed in Fig. 9 could be a consequence of a characteristic release or reloading of stress correlated to the interevent times, similar to predictions of the elastic rebound theory [114] and related earthquake models [104]. Figure 10(b) shows the autocorrelation function (ACF) of the sequences of  $\sigma_y(t^+)$  and  $\sigma_y(t^-)$ , respectively, for a pair of loose and dense assemblies with similar simulation parameters. Since the macromechanics of the system are relatively

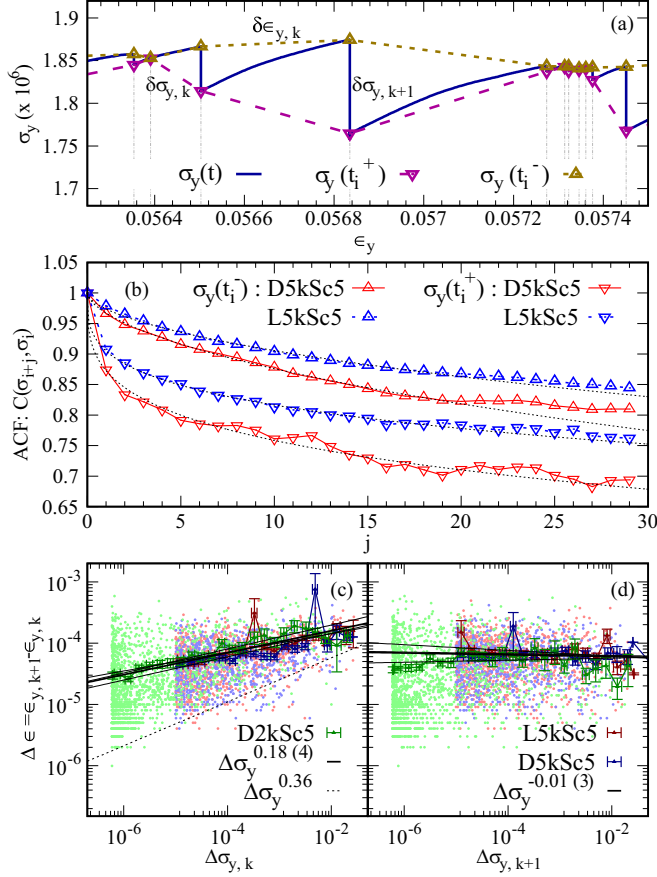


FIG. 10. (a) The macromechanical evolution of stress ( $\sigma_y$ ) vs strain ( $\epsilon_y$ ) (blue line). The dashed and dotted lines connect the values of stress on the onset ( $t^-$ ) and at the end ( $t^+$ ) of each avalanche  $i$ , respectively, for visual purposes. (b) Autocorrelation functions for the sequence of  $\sigma_y(t^-)$  and  $\sigma_y(t^+)$ , respectively. Lines represent best fits to a stretched exponential decay over the interval  $j \in [1, 30]$  (c, d) Scatter plots of the relations between the size of the (c) previous and (d) next avalanche ( $\Delta\sigma_y$ ) and the interevent strain  $\Delta\epsilon_y$  for three different simulations. Conditional averages represented in colored lines and linear fitting in black. The dashed line in (c) represents an empirical minimal loading period  $\Delta\epsilon \sim \Delta\sigma_y^{0.36(8)}$ .

smooth at the long range, as shown in Fig. 1, both autocorrelations persist for long times and remain at significant positive values over the shown range. In particular, correlations decay to a good approximation as a stretched exponential  $C \approx A \exp(-j^\xi)$  for  $j < 30$  with  $\xi = 0.598(16)$  for  $\sigma(t^-)$  and a faster  $\xi = 0.317(18)$  for  $\sigma(t^+)$ . Therefore,  $\sigma(t^-)$  values are significantly more persistent than  $\sigma(t^+)$ , suggesting that the state triggering the avalanches is more regular than the state arresting it. This hypothesis is confirmed by a comparison between the scatter plots of  $\Delta\sigma_{y,k}$  and  $\Delta\sigma_{y,k+1}$  as a function of  $\Delta\epsilon_y$  [Figs. 10(c) and 10(d)]. The duration of an interevent loading time does not affect the size of the next avalanche [Fig. 10(d)]. Instead, the size of an avalanche correlates with the next interevent loading time [Fig. 10(c)]. Specifically, after an event with stress drop  $\Delta\sigma_y$ , the system needs to load a characteristic minimum amount of strain  $\Delta\epsilon^{\min} \propto \Delta\sigma_y^{0.36}$  to trigger the next avalanche. This so-called time predictability [115] is consistent with the lack of short interevent times

[Fig. 9(a)]. In terms of the SES representation, and at least for the testing procedure adopted in this paper, the upper values of stress, i.e.,  $\sigma(t^-)$ , represent a better candidate for an objective reference state, and can be associated with the SES. The fact that the interevent times are correlated with their preceding events implies that typically the avalanches can be considered as excursions bringing the system away from the critical SES limit towards more stable configurations. The following loading has then a tendency to return the system to the SES.

We have shown that both distributions of avalanche sizes and interevent times are stationary once the SES is reached. On the other hand, the effective macroscopic Young's moduli  $E_y := \dot{\sigma}_y(\epsilon_y)$  within the SES is nonstationary and evolves towards the steady state in nonunique evolutionary paths (Fig. 1). This implies that a time dependence exists in the average stress reloading amount between consecutive avalanches [ $\langle \Delta\sigma_y^r \rangle := \langle \sigma_{y,k}(t^-) - \sigma_{y,k-1}(t^+) \rangle$ ] or the avalanche rates ( $r := N_{\text{aval}}/\Delta\epsilon_y$ ), even within the SES. To verify this hypothesis we evaluate such average reloading sizes in addition to the effective elastic modulus ( $\hat{E}_y := \Delta\sigma_y/\Delta\epsilon_y$ ) and average avalanche sizes [ $\langle \Delta\sigma_y \rangle := \langle \sigma_{y,k}(t^+) - \sigma_{y,k}(t^-) \rangle$ ] in relatively broad intervals of strain, i.e., driving, of  $\Delta\epsilon = 0.005$  containing around 70–100 avalanches each. We build a catalog considering all strain intervals in L5kSc5 and D5kSc5 within the SES together, since the input parameters are similar and include a large variability in  $E_y$ , mostly positive in L5kSc5 and mostly negative in D5kSc5 (see Fig. 1). We report the following Pearson correlation coefficients with respect to  $\hat{E}_y$ :

$$\rho_{\hat{E}_y, r} = 0.37, \quad \rho_{\hat{E}_y, \langle \Delta\sigma_y^r \rangle} = 0.30, \quad \rho_{\hat{E}_y, \langle \Delta\sigma_y \rangle} = 0.058, \quad (5)$$

the latter being effectively null. Therefore, we argue that the effective macroscopic Young's modulus is determined by the rate of avalanches and the reloading between avalanches in a way that low rates and high stress reloading correlate with positive effective moduli, while the characteristic size of avalanches is effectively constant, as already argued in Sec. III B. Some of the issues pertaining to time averaging such metastable quasistatic behaviors are discussed in Ref. [116].

#### IV. DISCUSSION

Nonlinear mechanics and avalanches in amorphous solids are often studied under the lens of AQS *shear* driving. Both atomistic and coarse-grained simulations usually consider overdamped systems of soft particles, usually modeled with attractive LJ potentials in discrete element models, returning short-range or far-field homogeneous stress transfer functions in a coarse-grained representation, either isotropic when considering interactions along the maximum shear plane [12,34], or polar Eshelby inclusions, when considering off-plane interactions [33,117,118]. The discrete element simulations of compact granular assemblies presented here differ from some of the previous considerations. Most notably, the system is driven by biaxial compression instead of shear, particles have inertia, and the stress distribution is channeled in complex force-chain networks resulting in highly disordered long-range interactions.

### A. Biaxial compression

Biaxial and triaxial compression experiments [97,100,119–121], and numerical simulations [89,122] such as the ones presented in this paper, serve as analogs for geomechanical processes. Mechanics at the mesoscale are dominated by internal shear processes introduced by residual deviatoric stresses at contact points. The correspondence with macroscopic shear is especially clear when activity is localized in a shear band [100,120,123] (see deformation of D5kSc5 in Fig. 1) but not so much when deformation is homogeneously distributed within the sample (L5kSc5 in Fig. 1). Avalanche statistics shown in previous sections appear to be independent of internal details once the system reaches the SES, whether the system exhibits softening behavior associated with localized failure (e.g., in the case of D5kSc5), or monotonic hardening leading to diffuse failure (e.g., in the case of L5kSc5). This suggests that the similarities in avalanche statistics are linked to particle scale mechanisms, such as frictionally arrested stick-slip events and force-chain buckling, rather than the coarse-grained elastoplastic macromechanics [124]. On the other hand, the introduction of soft, instead of fixed, lateral walls affects the energy partition of the system dynamics in general (Fig. 3) and the avalanche energy budget in particular. For purely strain-controlled loading programs, such as in constant-volume tests, an average proportionality is reported between  $D$  and  $\Delta\sigma$  [16,17]. In our paper presented here, the equivalence between  $D$  and  $\Delta U$ , and thus the proportionality between the stress drop and the energies, does not stand, because of the free production of lateral work  $W_x$ . Specifically, Fig. 4 shows that such a proportionality is maintained in  $\Delta U$  and, therefore, lost for  $D$  in general. Recalling the different scaling exponents in  $\Delta U^* \propto \sigma_x^{1.85}$  and  $W_x \propto \sigma_x$ , the equivalence  $\Delta U \approx D$  is asymptotically recovered at high confining pressures, given  $D = \Delta U + W_x \approx \Delta U$ .

### B. Effect of inertia and the pseudogap

Recent experiments in granular aggregates reported interevent time distributions consistent with triggering [101]. Inertia is known to affect statistics of both avalanche sizes and temporal correlations and could potentially constitute a mechanism of triggering explaining such observation. The relatively slow dissipation of the kinetic energy with respect to the stress drops we observe (see Fig. 3) might trigger secondary avalanches in the form of new spikes in  $\dot{U}(t)$  and  $E_K(t)$ . Similar phenomena have been reported in the signal profiles of acoustic emission events during the uniaxial compression of concrete samples [125]. We do observe, in rare occasions, a double peak in the kinetic energy within the same avalanche profile (not shown). Nevertheless, given the selected AQS driving protocol and low values of  $K_r$ , we can be certain that such double peaks are absorbed in a single avalanche event, recovering a practical independence between avalanches under the definition suggested in Ref. [126]. No evidence of self-excitation is found in either the Poisson-rejection test [Fig. 9(c)] or the distribution of interevent times shown in Fig. 9(b), which exhibits an exponential decay. In contrast, we report a deficit of short interevent times linked to regularity in the macromechanical state of the system at the onset of an avalanche (Fig. 10). This indicates that the

process has a certain time predictability [115], well identified as a characteristic minimum recharging strain as represented in Fig. 10(c).

This regularity of interevent times is predicted by finite-size effects as considered in some earthquake hazard assessment frameworks [127]. In small systems, all avalanches dissipate macroscopic fractions of elastic energy, causing longer reloading times after large avalanches. This effect disappears in the thermodynamic limit, where all subcritical and critical avalanches are massless. Alternatively, a similar quasiperiodic behavior is predicted in elastoplasticity by the presence of a so-called pseudogap in the density of residual stresses, i.e., the local stress differences to failure through different mechanisms, usually represented on a coarse-grained scale [22,33,41,47,48,117]. Rather than a *gap*, i.e., absence of small residual stresses ( $x$ ), the pseudogap is characterized by a power-law decay in the density of low values attributed to the nonmonotonous evolution of residual stresses towards the stability limit which corresponds to an absorbing boundary in a stochastic process representation [47]:

$$N(x) \sim x^\theta \quad \text{with } \theta > 0. \quad (6)$$

The pseudogap introduces a characteristic delay in the interevent times between consecutive avalanches, defined here as the strain  $\epsilon_y$  needed to activate the lowest  $x$  value in Eq. (6), and rendering the Weibull renewal behavior [22]:

$$P(\Delta\epsilon) = \frac{1+\theta}{\langle\Delta\epsilon\rangle} \left(\frac{\Delta\epsilon}{\langle\Delta\epsilon\rangle}\right)^\theta \exp\left[-\left(\frac{\Delta\epsilon}{\langle\Delta\epsilon\rangle}\right)^{\theta+1}\right]. \quad (7)$$

Such a behavior is shown in Figs. 9(a) and 9(b) as the black lines. Recent studies in discrete element [109], finite element [43], and conceptual [48] models identified an additional system-size dependent plateau overlapping with the pseudogap, which vanishes in the thermodynamic limit. According to these results, quasiperiodicity would be more prominent in large systems while interevent times in small systems would be better described by a Poisson process. This system-size dependence, opposite to the expectations from finite-size effects, qualitatively agrees with our results presented in Fig. 9 and is numerically verified in the Supplemental Material [83] (Figs. S2 and S5). However, the analysis presented in Fig. 9 is insufficient to determine the system-size dependency of the plateau or the exponent  $\theta$  defining the pseudogap following the analysis presented in Ref. [41]. Instead one can use hyperscaling relations to address the latter as we discuss in Sec. IV E. Yet, Fig. 9 shows that the distribution of short interevent times is close to the expectations of the Weibull renewal model with an exponent between 0.5 and 1, with a generally higher exponent, suggesting a more prominent pseudogap in the large samples [Fig. 9(a)]. At the region of long interevent times, the distributions are better reproduced by the Poisson hypothesis instead [Fig. 9(b)]. This might indicate a change in the distribution of  $x$ , marking the end of the power-law regime described by Eq. (6).

Finally, inertial effects were found to affect the critical exponents determining bulk avalanche statistics in discrete element simulations of LJ particles [16,17,88,128]. This feature could as well be related to the observation that the states triggering avalanches, herein considered to be constrained to

a SES manifold, are more regular than the arrested states (see Sec. III D). The kinetic energy introduced by “fast” external driving is known to affect mechanical equilibrium [78–80,129]. We propose that the SES represents a collection of metastable configurational limits to the mechanical equilibrium that are marginally reachable under quasistatic conditions [75]. When an avalanche is initiated at the SES, the excess kinetic energy prevents the relaxation of the system at a fragile state, e.g., the same configurational state at the onset of the avalanche. The configurational state arresting the avalanche, which is reached at  $t_0 + T$ , needs to be stable while the system still retains a relatively high amount of kinetic energy (see Fig. 3). Since the excess of kinetic energy is dampened below  $K_r$  before resuming the driving, we believe that the particle inertia during the avalanche has to affect the distribution of residual stresses, and the properties of the pseudogap. This idea of stability *overshooting* was conceptually captured in a depinning model with transient effects predicting a system-size dependence on the time predictability of transitions [81] qualitatively similar to the one observed in the pseudogap, verified at the stiff particle limit in our simulations. A similar effect is reproduced by the addition of *dynamic weakening* in some EPMs, and the slip mean-field theory in particular [35]. However, the effect on avalanche sizes is far from being trivial. Numerical studies with LJ particles found nonmonotonous relations between critical exponents and inertia, and regimes with characteristic and time-predictable avalanches [17], the latter being predicted in slip mean-field theory as well [35].

### C. Stiff granular particles

Apart from particle inertia, most coarse-grained EPMs also overlook the nonlinearity of the internal stress fields [51–53]. The hypothesis of the uniformity in the stress propagation enabling the coarse-graining in elastoplastic models is known to fail in the presence of stiff particles [3]. As mentioned, stress distribution in granular media is governed by the structural topology of contact points, generating complex force-chain networks, highly susceptible to small variations of stress. A crossover between fragile and amorphous materials has long been suggested to exist as a function of softness or *deformability* [26], even in the absence of attractive particle potential [21,27]. The variation in the power-law exponents in Fig. 8 is in agreement with such a transition (see Sec. IV E for a more detailed discussion). Recent studies have suggested the introduction of internal structural variables such as compactivity [61,63,130], angoricity [62,64,65,131], or the more recent concept of keramicity [65–67] complementing the stress-strain formulation traditionally considered in EPMs. Based on our results, we propose the SES concept as an alternative micromechanical representation of the state of granular materials determined by the structure of the internal contact network rather than the macromechanics [77].

### D. Interpretation of avalanche sizes in terms of elastoplasticity

The EPM formulation separates plastic avalanche events from the elastic deformation caused by the AQS driving. Although the separation of temporal scales is not as straight-

forward in discrete element simulations, one can still find a correspondence between the variables defining avalanches in the different modeling approaches. In this sense, we are interested in the conceptual picture provided by the slip mean-field theory, which is arguably the simplest EPM framework to characterize avalanche statistics, and has shown good agreement with the statistics of avalanches in granular assemblies sharing in particular the same universal critical exponents [12,13,39]. In the slip mean-field theory, the avalanches are measured in terms of a global signal [ $v(t)$  in short intervals] which accounts for the collective velocity of displacement of the constituting elements (also known as cells) of the model, and is proportional to the rate of external stress drop under strain driving. Henceforth, the size  $S := \int_{t_0}^{t_0+T} v(t) dt$  of an avalanche of duration  $T$  starting at time  $t_0$  is a measure proportional to stress drop. Similarly,  $E := \int_{t_0}^{t_0+T} v^2(t) dt$  is proportional to the total kinetic energy dissipated, and  $E_m := v_{\max}^2(t) dt$  is proportional to the maximum peak of the instantaneous kinetic energy within the avalanche. In order to compare the results in discrete element models with the expectations from elastoplasticity, we first need to establish reliable links between the avalanche sizes defined within the conceptual framework proposed in the slip mean-field theory and the measures defining avalanche sizes in discrete element models.

Considering EPM formulations, it is natural to assume an approximate proportionality between elastic energy and small deformations. Given its mean-field nature, the slip mean-field theory assumes an exact proportionality [ $\dot{\sigma} \propto v(t)$ ] during avalanches, and predicts an approximate proportionality with the elastic energy release. This is consistent with the observed proportionality between internal elastic energy  $\Delta U$  and  $\Delta\sigma_y$  illustrated in Fig. 4. We adopt the strain drop as the avalanche size  $S := \Delta\sigma_y$ , following the convention in Refs. [16,17]. Moreover, to remain consistent with slip mean-field theory, the avalanche duration  $T$  has been defined in this paper to be the time interval of the potential energy release, which is virtually indistinguishable from the time interval of the stress drop.

Although  $K := E_K^{\max} - K_D$  represents the peak in our simulations and, hence, it is reminiscent of  $E_m$ , the dissipation process is significantly slower compared to the rise of kinetic energy. In contrast, slip mean-field theory considers a strict overdamped limit where all inertial effects are instantly dissipated. Therefore, we argue that the pick of kinetic energy  $K$  reached during the initial avalanche growth corresponds to the collective cumulative energy  $E$  in terms of slip mean-field theory. In Fig. 3(a) we observe a separation of temporal scales between the kinetic energy rise time, roughly matching the temporal interval ( $t_0, t_0 + T$ ), and the characteristic dissipation time [see the gray areas in Fig. 3(a)]. Almost no energy has been dissipated at  $T$ . We therefore adopt  $K \propto E$  in terms of the variables in slip mean-field theory. This assumption can be verified by comparing the values of  $K$  with an auxiliary avalanche variable  $\Delta(U^2) := \int_{t_0}^{t_0+T} dt (dU/dt)^2$  [see Fig. S6 in the Supplemental Material [83] representing the relation between  $\Delta(U^2)$  and  $K$ ]. If we assume a temporal proportionality between  $\dot{U}(t)$  and  $v(t) := dS/dt$ , for consistency  $(dU/dt)^2(t) \propto v(t)^2$ . Therefore the proportionality  $K \propto E$

implies  $K \propto \Delta(U^2)$ , as verified in Fig. S6. However, for the sake of completeness, in the next section we compare our results considering both  $K \propto E$  (herein referred to as model SMFT<sup>(1)</sup>) and  $K \propto E_m$  (SMFT<sup>(2)</sup>) to validate our hypothesis in light of the exponent values.

### E. Nonuniversal critical exponents

In the absence of self-excitation the spatial extension of avalanches serves as a proxy of local spatial correlations and, therefore, one can assess system susceptibilities from avalanche statistics. Since no divergence of activity rate is observed in the catalogs, criticality has to be linked to a divergence of characteristic scales in avalanche distributions. Hence the power-law distributions  $P(\Delta U)$  and  $P(K)$  reported in Sec. III B are a trademark of criticality. Close to criticality such distributions obey a scaling form:

$$\begin{aligned} P(\Delta U) d\Delta U &= \Delta U^{-\kappa} \Phi_{\Delta U}(\Delta U/\Delta U^*) d\Delta U, \\ P(K) dK &= K^{-\varepsilon} \Phi_K(K/K^*) dK, \end{aligned} \quad (8)$$

where  $\kappa$  and  $\varepsilon$  are the so-called critical exponents (Table II),  $\Phi_{\Delta U}$  and  $\Phi_K$  are universal scaling functions (often in the form of an exponential cutoff), and  $\Delta U^*$  and  $K^*$  are characteristic avalanche sizes, related to the correlation length. When approaching criticality, the correlation length diverges such that for any finite system it eventually takes on the system size value. Therefore,  $\Delta U^* \sim L^{d_f}$ , where  $L$  is the lateral size of the system. Considering that the system stays close to criticality, at the stiff particle limit ( $\sigma_x = 10^5$ ) our simulation results are consistent with  $d_f \approx 1$  (see Sec. III B). Values  $d_f \sim 1$  have been commonly found in previous studies [15] and discrete element simulations [17,20]. Other finite element simulations [128] reported a dependence of exponents  $d_f$  and  $\theta$  on a damping coefficient  $\Gamma$  that could, potentially, include the contribution of confining pressure to the avalanche propagation. Here for the sake of the discussion we will consider  $d_f$  to be invariant to  $\sigma_x$ .

In slip mean-field theory, the relations between the average sizes, energies, and durations take the following power-law form (see Ref. [36]):

$$\begin{aligned} \langle T|S \rangle &\sim S^{\varsigma\nu z} & \text{where } \varsigma\nu z &= 1/2, \\ \langle E|S \rangle &\sim S^{2-\varsigma\nu z} & \text{where } 2-\varsigma\nu z &= 3/2, \\ \langle E_m|S \rangle &\sim S^{2\varsigma\rho} & \text{where } 2\varsigma\rho &= 1. \end{aligned} \quad (9)$$

Considering the proportionality between differential deformation and avalanche sizes, one can prove that the monotonic driving brings the system towards the aforementioned stationary SOC flow regime around  $\sigma_c$  with scale-free statistics, leading to Eq. (1). Considering the exponents above, and the proportionality between  $\Delta U$  and  $S$ , criticality imposes power-law distributions with the following exponent relations (see Ref. [36]):

$$\begin{aligned} P(S) &\sim S^{-\kappa} & \text{where } \kappa &= 3/2, \\ P(E) &\sim E^{-1-\frac{\kappa-1}{2-\varsigma\nu z}} & \text{where } 1+\frac{\kappa-1}{2-\varsigma\nu z} &= 4/3, \\ P(E_m) &\sim E_m^{-\frac{1+\mu}{2}} & \text{where } \frac{1+\mu}{2} &= 3/2. \end{aligned} \quad (10)$$

In Table II we compare our results with the predictions of slip mean-field theory in both interpretations of  $K$  (models SMFT<sup>(1)</sup> and SMFT<sup>(2)</sup>) and the typical range of exponents reported in numerical studies considering similar relations between observables [3,42,84]. We notice that studies investigating the effect of dimensionality reported no significant differences between 2D and three-dimensional systems [17,42]. The most remarkable observation is that the exponents in our simulations are nonuniversal. When the confining pressure is low, or contacts are relatively stiff ( $\sigma_x = 10^5$ ), the granular compact assemblies in all three exponents  $\kappa$ ,  $\varepsilon$ , and  $\gamma$  are consistent with SMFT<sup>(1)</sup>, i.e., considering  $K = E$ , although exponents  $\kappa$  and  $\gamma$  are slightly higher than expected in slip mean-field theory. Notice that this agreement holds for both loose and dense assemblies, even when the macromechanical evolutionary path is different from slip mean-field theory in the latter. The correspondence with the predictions from the slip mean-field theory is progressively lost for higher confining pressures. In the extreme case of  $\sigma_x = 10^7$ , the exponent  $\gamma = 1.48(7)$  is still close to the mean-field prediction, and in agreement with recent results in 2D EPM simulations (e.g.,  $\gamma \approx 1.45$  in [42]). However,  $\kappa$  and  $\varepsilon$  decrease towards values close to 1.0. Note that  $\gamma$  plays a minor role in the relation between  $\kappa$  and  $\varepsilon$  when both exponents are close to 1 [see Eq. (4)]. The exponents  $\kappa$  and  $\varepsilon$  at high confining pressures, which depart from predictions from the slip mean-field theory, are closer to the predictions from EPMs within 2D lattices, where lower exponents are reported:  $\kappa \sim 1.28$  and  $\varepsilon \sim 1.20$  [42,84];  $\kappa \approx 1.1-1.2$  [132] or even down to  $\kappa = 0.98(1)$  [20]. The ranges found in  $\kappa$  are also consistent with previous reports comparing experiments and discrete element simulations [133], and simulations with variable heterogeneity [134]. It has been argued that this change of behavior can be interpreted as a transition between different universality classes [42]. In that case, our results might indicate a transition between conceptual limits.

To sum up, the statistics of avalanches in noncohesive assemblies of stiff particles are relatively close to the expectations of the slip mean-field theory, especially for the most robust exponent  $\varepsilon$ , whilst the avalanches for soft particles are close to the predictions of elastoplasticity with short-range interactions or geometric propagators. This might signal a dependence to softness of the propagation of interactions, as already predicted [26] and observed in impact experiments [135]. A plausible explanation is that the force chain formations are more prominent at the stiff-particle limit, and as such, the effective interactions are long-ranged [135] and avalanches can be represented in terms of isotropic homogeneous and independent branching processes. In contrast, at the soft-particle limit, the deformability of particles accommodates the stress variation in finite structures well modeled by Eshelby-like propagators in the coarse-grained mesoscale. Therefore, we argue that the nonequilibrium statistical physics of fragile matter do not significantly differ from those of amorphous materials with attractive potentials as long as correlations, or influence of force-chain structures, are damped at short length scales. Similar parameter-dependent exponents have been found in other simulations and linked to changes in the effective dimension of avalanche location [89,136]. From standard renormalization theory it is known that, in general,

effective system dimensions and the range of interactions condition the universality class, i.e., the critical exponents. The behavior at intermediate softness could therefore represent a crossover phenomenon, giving rise to an “effective” set of exponents that would depend on the system size.

Finally, following the hyperscaling relation between avalanche-size distribution and the pseudogap [47],

$$\kappa = 2 - \frac{\theta}{\theta + 1} \frac{d}{d_f}. \quad (11)$$

Assuming  $d_f$  as constant, the exponent  $\theta$ , determining the distribution of residual stresses, Eq. (6), and interevent times, transitions from  $\theta \approx 0.5$  for stiff particles to  $\theta \approx 1$  for soft particles if we use the fitted values of  $\kappa$  from Table II. These two extreme cases (represented in Fig. 9) are in agreement, respectively, with the expected  $\theta = 0.5$  found in mean-field models [47] and  $\theta \approx 0.9-1$  found in discrete element simulations considering LJ potentials [20,84,132]. Overall, we observe a general correspondence between the exponents fitted at low confining pressure with the predictions of the slip mean-field theory, and we recover the usual ranges of values found in EPMs and other simulations of amorphous materials at higher confining pressures.

#### F. Avalanche statistics on the SES are stationary and scale free

The interpretation of the SES manifold as a stability limit solves the problem of the nonmonotonous evolution from a macroscopic point of view, once structural configurational aspects are taken into account. Beyond that, and as far as we can tell, the SES defines the “state” of the assembly where avalanche statistics is nondegenerated. Upon reaching the SES at different stress values, and once the variations in the avalanche activity rate are accounted for, no difference in the statistics of avalanches is observed (Fig. 5). The distributions of avalanche sizes are virtually identical, independently of the  $\sigma_y$  values, the evolutionary path, and the initial configuration. Focusing on the result at the stiff-particle limit, and despite the complexity of the internal processes involved, the macromechanical evolution of loose assemblies, such as L5kSc5 in Fig. 1, is in agreement with the predictions of the slip mean-field theory [Eq. (1)]. In particular, the predictions from the slip mean-field theory extend way beyond the proximity-limit of  $\sigma_c$ , and apply to the entire observation interval. In contrast, initially dense assemblies, such as D5kSc5 in Fig. 1, display the typical peak in stress and postpeak strain softening which is not captured by Eq. (1) or the scaling relations in the slip mean-field theory. However, once the SES is reached, the distributions in Fig. 5 are already compatible with the scale-free behavior in the slip mean-field universality class, besides the aforementioned finite-size effects, way before the steady-state flow regime. Therefore, we argue that the SES is not only an attractor manifold to the internal state of the system, but might as well correspond to the SOC state [29–32] from the perspective of out-of-equilibrium statistical physics. This is also demonstrated in Ref. [77] where a preliminary measure for a distance to criticality is suggested based on the concept of the SES. Further studies are nevertheless necessary to determine whether the SES is indeed an exact representation of avalanche criticality or yet another approximation.

This question can be addressed in principle through a finite-size scaling analysis of avalanche distributions in terms of the parameters representing the distance to SES. Yet, it is a computationally cumbersome task if one wants to obtain statistically reliable conclusions [42], which remains a challenge for the future.

#### V. CONCLUSIONS

We presented a statistical analysis of kinetic avalanches recorded during discrete element simulations of granular assemblies with elastic potentials under AQS conditions. It showed that criticality, in the form of power-law statistics, is degenerated in the space of the commonly used macroscopic state variables such as stress and strains. Instead, internal measurements, such as the fabric anisotropy, the rigidity ratio, and average coordination number, in which the manifold herein referred to as the stable evolutionary state is defined, appear to provide a more appropriate representation of criticality, and closeness to criticality, in terms of avalanche statistics and susceptibilities. In particular, we have presented evidence that points towards the existence of a link between (i) the SES, identified as an attractor of the evolution of granular systems in the space of internal measurements [77], and (ii) criticality characterized by a divergence of susceptibilities and scale-free avalanches. Therefore, we argue that the SES is itself a SOC state, representing a basin of attraction to the state of the system with scale-free independent avalanches before reaching the stationary flow regime.

We interpret the observed time predictability as evidence that the SES corresponds to a stability limit under AQS conditions. In terms of the residual-stress formulation, we conjecture that the SES, determined by the potential energy landscape, dominates the dynamics during driving as considered in EPMs, although the high susceptibility of the system might introduce nonaffine stress rearrangements through the force-chain network. Conversely, based on the higher correlation between states at the onset of avalanches than between states arresting avalanches, we believe that the avalanche propagation is strongly affected by the transient kinetic energy in underdamped inertial systems. Therefore, the stability of the assembly during the compression process is determined by the combined effect of equilibrium constraints governing the quasistatic stability and the transient addition of kinetic energy during avalanche propagation. Testing this hypothesis further remains a challenge for the future, potentially involving simulations with alternative control protocols, the inclusion of thermal effects, and/or the tuning of frictional and damping parameters. On the other hand, the reported avalanche interevent times are compatible with the power-law pseudogap hypothesis, rendering a Weibull renewal process for large system sizes, while the Poisson hypothesis is still valid for small systems. This is in agreement with the possible existence of a system-size dependent plateau in the distribution of residual stresses recently discussed in the literature [43,48,109].

Despite the particular aspects of our simulations, the reported avalanche statistics do not differ significantly from the expectations of EPMs and can, in fact, bridge the gap between the depinning universality class associated with the slip

mean-field theory and the extended nonuniversal exponents in yielding [41] that could represent a crossover towards a new universality class of elastoplasticity and, therefore, be invariant with respect to the dimensionality of the system [42]. We found that the external stress drop ( $\Delta\sigma$ ) is proportional to the internal energy drop  $\Delta U$  and a good proxy for the internal displacement, or  $S$  in terms of the slip mean-field theory [12,36]. The peak of kinetic energy ( $K$ ) serves as a good proxy for the avalanche energy  $E$ . The observed exponents characterizing the critical state are nonuniversal and display a transition from (i) the expected values in the slip mean-field theory, for stiff particles or low confining pressures in our simulations, to (ii) the lower exponents observed in 2D simulations of amorphous materials [20,42,84,132], for soft particles or high confining pressures in our simulations. This could be linked to the known change in spatial distribution and anisotropy of correlations in the two limits, which depends on the structure and robustness of the internal force-chain network connecting the contact points [26,135]. In particular, for stiff particles, small displacements in a single contact can propagate through the force chain and span the whole system, resulting in a homogeneous and isotropic long-ranged response at the coarse-grained scale, similar to the interactions in the slip mean-field theory. In contrast, soft particles accommodate variations of stress at a short-range scale, reminiscent of the typical Eshelby inclusion modeled in 2D EPMs [118]. On the other hand, inertial effects are found to depend on stiffness and are known to affect avalanche statistics as well [16,17,88,128]. Finally, the relation between stiffness and the universality class is further reinforced by the indirect estimation of the exponent  $\theta$  defining the distribution of residual stresses, which satisfies the expectations of mean-field models [47] for stiff particles and 2D EPMs for soft particles [20,84,132].

To summarize, based on our results we propose a static stability limit as a candidate for a SOC state reached before the traditional flow regime, and a link between the collection of critical exponents defining the critical state and the stiffness of the particles. These two conjectures should serve as a starting point to extend our understanding of the discussed nonuniversality in the deformation of amorphous materials, and the role of the internal structure and its dynamics during the deformation. Indeed, we strongly believe that this might be a fundamental aspect to understand the fit of fragile matter within elastoplastic theory.

#### ACKNOWLEDGMENTS

We thank Daniel Korchinski for fruitful discussions. J.B. acknowledges financial support from the Santander Universities, and the AXA Research Fund through the project RheMechFail. This work was financially supported by the Natural Sciences and Engineering Research Council of Canada. We thank Mark Robbins for insightful discussions.

#### APPENDIX A: EFFECTIVE SCALING OF $\Delta U$ WITH $\sigma_x$

Following a linear elastic relation, the change in elastic energy can be written in terms of the wall stresses and the

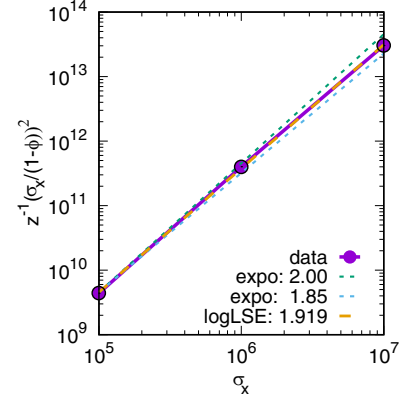


FIG. 11. Effective scaling of the term  $\sigma_x/(1-\phi)^2/z$  given the corrections in the dependencies of  $\phi(\sigma_x)$  and  $z(\sigma_x)$ . The best fit is given by exponent 1.91(4) (yellow dashed line). Results with exponent 2 (uncorrected) and 1.85 (scaling observed in Fig. 4) are shown for comparison.

normalized stress released:

$$\Delta U = V \left( \frac{\sigma_y}{\sigma_x} \frac{1}{E_y} - \frac{\nu_{xy}}{E_x} \right) \sigma_x^2 \frac{\Delta\sigma_y}{\sigma_x}, \quad (\text{A1})$$

where  $V := l_x l_y \propto N\pi(r^2)/(1-\phi)$  is the system's volume with  $\phi$  being the porosity,  $E_x$  and  $E_y$  the macroscopic Young's moduli, and  $\nu_{xy}$  the associated Poisson ratio. The macroscopic Young's moduli also depend on coordination number ( $Z$ ) and the total volume,  $E \propto ZV^{-1} \propto Z(1-\phi)$  [137,138]. Taking into account that the stress ratio ( $\frac{\sigma_y}{\sigma_x}$ ) fluctuates in no more than 1/3 of its average value within the catalog (Fig. 1), Eq. (A1) can be simplified to give the following scaling:

$$\Delta U \propto Z^{-1}(1-\phi)^{-2} \sigma_x^2 \frac{\Delta\sigma_y}{\sigma_x}. \quad (\text{A2})$$

The remaining mismatch between the exponent 1.85(5) used in the scaling of Fig. 4 and the exponent 2 in Eq. (A2) is found in an effective relation between  $Z(1-\phi)^{-2}$  and  $\sigma_x$  which renders  $\Delta U \propto \sigma_x^{1.91(4)} \Delta\sigma_y/\sigma_x$  (see Fig. 11).

#### APPENDIX B: EXPONENT ESTIMATION BY MAXIMUM LIKELIHOOD

We estimate the power-law exponents from distributions of the type of Eq. (2) by maximizing the likelihood function  $\mathcal{L}(\gamma) := \prod_{\{X_i\}} p_x(X_i|\gamma)$ . Since the scale-free behavior of the avalanches is limited by finite-size effects, instead of a pure power-law distribution we consider a truncated power-law model, and the exponents are estimated within a restricted range  $(x_l, x_h)$ . We select a reasonable power-law range excluding the lower and upper end of the distribution. In order to avoid any additional effect related to the shape of the scaling function  $\Phi_x(x/x^*)$  we select the same intervals for all distributions of  $\tilde{K}$  and  $\tilde{\Delta U}$ :

$$\begin{aligned} -13.05 < \log_{10}(\tilde{\Delta U}) < -12.05, \\ -11.3 < \log_{10}(\tilde{K}) < -9.8, \end{aligned} \quad (\text{B1})$$

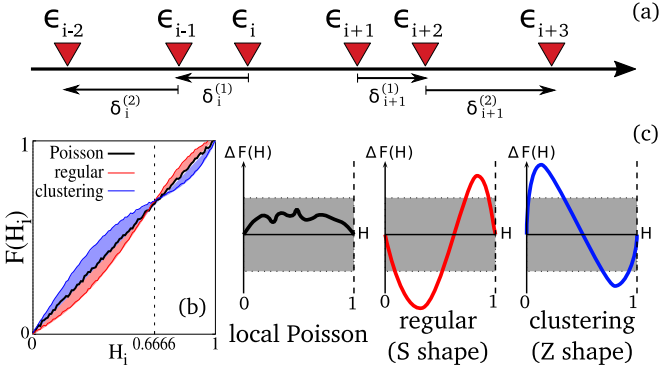


FIG. 12. Schematic representation of the Bi test. (a) Examples of  $\delta^{(1)}$  and  $\delta^{(2)}$  for two events:  $i$  and  $i + 1$  represented in the time, i.e.,  $\epsilon_y$ , line. (b) Expected cumulative distribution for a local Poisson, a regular process, and a process with clustering. (c) Expected results of a KS test. The gray bar represents a confidence interval for rejection.

as represented in Fig. 7. For simulations at high confining pressures ( $\sigma_x \geq 10^6$ ) we increase the fitting ranges to

$$\begin{aligned} -13.55 < \log_{10}(\widetilde{\Delta U}) < -12.05, \\ -11.8 < \log_{10}(\widetilde{K}) < -9.8, \end{aligned} \quad (\text{B2})$$

to take advantage of the extended power-law regime to lower values (see individual distributions and selected estimation ranges in Figs. S3 and S4 of the Supplemental Material [83]).

The maximum likelihood estimation is performed following the recipe in Ref. [86]. Given a set of  $N$  observations  $\{X_i\}$  within an evaluation interval  $(x_l, x_h)$ , the estimated exponent  $\hat{\gamma}$  is given by the numerically solvable equation

$$\sum_{\{X_i\}} \ln X_i = \frac{x_h^{1-\hat{\gamma}} \ln x_h - x_l^{1-\hat{\gamma}} \ln x_l}{x_h^{1-\hat{\gamma}} - x_l^{1-\hat{\gamma}}} - N \frac{1}{1-\hat{\gamma}}. \quad (\text{B3})$$

### APPENDIX C: TEST FOR INDEPENDENCE OF INTEREVENT TIMES

The so-called Bi test [113] is used to assess the validity of a local Poisson model based on the statistical properties of consecutive interevent times. We consider  $\delta_i^{(1)}$  as the shortest of the intervals preceding or following each event  $i$ . In terms of strain,

$$\delta_i^{(1)} := \min(\epsilon_{y,i+1} - \epsilon_{y,i}, \epsilon_{y,i} - \epsilon_{y,i-1}). \quad (\text{C1})$$

We consider  $\delta_i^{(2)}$  as the next interevent time in the same temporal direction of  $\delta_i^{(1)}$ :

$$\begin{aligned} \delta_i^{(2)} &:= \epsilon_{y,i-1} - \epsilon_{y,i-2} & \text{if } \delta_i^{(1)} = \epsilon_{y,i} - \epsilon_{y,i-1}, \\ \delta_i^{(2)} &:= \epsilon_{y,i+2} - \epsilon_{y,i+1} & \text{if } \delta_i^{(1)} = \epsilon_{y,i+1} - \epsilon_{y,i}. \end{aligned} \quad (\text{C2})$$

See Fig. 12(a) for a schematic representation with the values for  $i$  and  $i + 1$ . Given the series of  $\delta_i^{(1)}$  and  $\delta_i^{(2)}$ , we build the statistical variable:

$$H_i = \frac{\delta_i^{(1)}}{\delta_i^{(1)} + 0.5\delta_i^{(2)}}. \quad (\text{C3})$$

If the process is locally Poissonian, we expect the  $H_i$  values to be uniformly distributed. In contrast, if the interevent times are more regular than expected, the distribution is peaked around  $H = 2/3$ , and if events are clustered together we observe an excess of  $H_i$  values at  $H \gtrsim 0$  and  $H \lesssim 1$  [Fig. 12(b)]. We use the KS test to reject the hypothesis that the events are independent, i.e., the point process can be modeled as a local or nonhomogeneous Poissonian. In case of rejection, we identify the nature of the correlations by visual inspection [Fig. 12(c)]. Regularity appears as a rotated S profile and clustering as a rotated Z profile. See Ref. [99] for further details.

- [1] J. P. Sethna, K. A. Dahmen, and C. R. Myers, *Nature (London)* **410**, 242 (2001).
- [2] E. K. Salje and K. A. Dahmen, *Annu. Rev. Condens. Matter Phys.* **5**, 233 (2014).
- [3] A. Nicolas, E. E. Ferrero, K. Martens, and J.-L. Barrat, *Rev. Mod. Phys.* **90**, 045006 (2018).
- [4] M. C. Miguel, A. Vespignani, S. Zapperi, J. Weiss, and J.-R. Grasso, *Nature (London)* **410**, 667 (2001).
- [5] M. Zaiser, *Adv. Phys.* **55**, 185 (2006).
- [6] N. Friedman, A. T. Jennings, G. Tsekenis, J.-Y. Kim, M. Tao, J. T. Uhl, J. R. Greer, and K. A. Dahmen, *Phys. Rev. Lett.* **109**, 095507 (2012).
- [7] G. Wang, K. Chan, L. Xia, P. Yu, J. Shen, and W. Wang, *Acta Mater.* **57**, 6146 (2009).
- [8] J. Antonaglia, W. J. Wright, X. Gu, R. R. Byer, T. C. Hufnagel, M. LeBlanc, J. T. Uhl, and K. A. Dahmen, *Phys. Rev. Lett.* **112**, 155501 (2014).
- [9] P. Schall, D. A. Weitz, and F. Spaepen, *Science* **318**, 1895 (2007).
- [10] Y. Hu, L. Shu, Q. Yang, W. Guo, P. K. Liaw, K. A. Dahmen, and J.-M. Zuo, *Commun. Phys.* **1**, 61 (2018).
- [11] Q. Rizzardi, G. Sparks, and R. Maaß, *JOM* **70**, 1088 (2018).
- [12] K. A. Dahmen, Y. Ben-Zion, and J. T. Uhl, *Nat. Phys.* **7**, 554 (2011).
- [13] D. V. Denisov, K. A. Lörcincz, J. T. Uhl, K. A. Dahmen, and P. Schall, *Nat. Commun.* **7**, 10641 (2016).
- [14] E. Berthier, J. E. Kollmer, S. E. Henkes, K. Liu, J. M. Schwarz, and K. E. Daniels, *Phys. Rev. Mater.* **3**, 075602 (2019).
- [15] C. Maloney and A. Lemaître, *Phys. Rev. Lett.* **93**, 016001 (2004).
- [16] K. M. Salerno, C. E. Maloney, and M. O. Robbins, *Phys. Rev. Lett.* **109**, 105703 (2012).
- [17] K. M. Salerno and M. O. Robbins, *Phys. Rev. E* **88**, 062206 (2013).
- [18] G. Parisi, I. Procaccia, C. Rainone, and M. Singh, *Proc. Natl. Acad. Sci. USA* **114**, 5577 (2017).
- [19] D. Zhang, K. A. Dahmen, and M. Ostojca-Starzewski, *Phys. Rev. E* **95**, 032902 (2017).
- [20] B. Shang, P. Guan, and J.-L. Barrat, *Proc. Natl. Acad. Sci. USA* **117**, 86 (2020).
- [21] E. Lerner and I. Procaccia, *Phys. Rev. E* **79**, 066109 (2009).
- [22] S. Karmakar, E. Lerner, and I. Procaccia, *Phys. Rev. E* **82**, 055103(R) (2010).

- [23] F. Gimbert, D. Amitrano, and J. Weiss, *Europhys. Lett.* **104**, 46001 (2013).
- [24] M. Pouragha and R. Wan, *Granular Matter* **18**, 38 (2016).
- [25] K. Karimi and J.-L. Barrat, *Sci. Rep.* **8**, 4021 (2018).
- [26] M. E. Cates, J. P. Wittmer, J.-P. Bouchaud, and P. Claudin, *Phys. Rev. Lett.* **81**, 1841 (1998).
- [27] A. J. Liu and S. R. Nagel, *Nature (London)* **396**, 21 (1998).
- [28] D. Bi, J. Zhang, B. Chakraborty, and R. P. Behringer, *Nature (London)* **480**, 355 (2011).
- [29] P. Bak and K. Chen, *Sci. Am.* **264**, 46 (1991).
- [30] K. Chen, P. Bak, and S. P. Obukhov, *Phys. Rev. A* **43**, 625 (1991).
- [31] S. Zapperi, K. B. Lauritsen, and H. E. Stanley, *Phys. Rev. Lett.* **75**, 4071 (1995).
- [32] N. W. Watkins, G. Pruessner, S. C. Chapman, N. B. Crosby, and H. J. Jensen, *Space Sci. Rev.* **198**, 3 (2016).
- [33] P. Hébraud and F. Lequeux, *Phys. Rev. Lett.* **81**, 2934 (1998).
- [34] Y. Ben-Zion and J. R. Rice, *J. Geophys. Res.: Solid Earth* **98**, 14109 (1993).
- [35] K. A. Dahmen, Y. Ben-Zion, and J. T. Uhl, *Phys. Rev. Lett.* **102**, 175501 (2009).
- [36] K. A. Dahmen, Mean field theory of slip statistics, in *Avalanches in Functional Materials and Geophysics*, edited by E. K. Salje, A. Saxena, and A. Planes (Springer, New York, 2017), pp. 19–30.
- [37] K. Dahmen, D. Ertaş, and Y. Ben-Zion, *Phys. Rev. E* **58**, 1494 (1998).
- [38] A. P. Mehta, K. A. Dahmen, and Y. Ben-Zion, *Phys. Rev. E* **73**, 056104 (2006).
- [39] D. A. Geller, R. E. Ecke, K. A. Dahmen, and S. Backhaus, *Phys. Rev. E* **92**, 060201(R) (2015).
- [40] E. I. Corwin, H. M. Jaeger, and S. R. Nagel, *Nature (London)* **435**, 1075 (2005).
- [41] J. Lin, A. Saade, E. Lerner, A. Rosso, and M. Wyart, *Europhys. Lett.* **105**, 26003 (2014).
- [42] Z. Budrikis, D. F. Castellanos, S. Sandfeld, M. Zaiser, and S. Zapperi, *Nat. Commun.* **8**, 15928 (2017).
- [43] D. Korchinski, C. Ruscher, and J. Rottler, [arXiv:2101.10688](https://arxiv.org/abs/2101.10688) (2021).
- [44] J.-C. Baret, D. Vandembroucq, and S. Roux, *Phys. Rev. Lett.* **89**, 195506 (2002).
- [45] G. Picard, A. Ajdari, and F. Lequeux, and L. Bocquet, *Phys. Rev. E* **71**, 010501(R) (2005).
- [46] E. Agoritsas, E. Bertin, K. Martens, and J.-L. Barrat, *European Phys. J. E* **38**, 71 (2015).
- [47] J. Lin and M. Wyart, *Phys. Rev. X* **6**, 011005 (2016).
- [48] E. E. Ferrero and E. A. Jagla, *Soft Matter* **15**, 9041 (2019).
- [49] D. Rodney, A. Tanguy, and D. Vandembroucq, *Modell. Simul. Mater. Sci. Eng.* **19**, 083001 (2011).
- [50] B. Miller, C. O’Hern, and R. P. Behringer, *Phys. Rev. Lett.* **77**, 3110 (1996).
- [51] D. M. Mueth, H. M. Jaeger, and S. R. Nagel, *Phys. Rev. E* **57**, 3164 (1998).
- [52] C. h. Liu, S. R. Nagel, D. A. Schecter, S. N. Coppersmith, S. Majumdar, O. Narayan, and T. A. Witten, *Science* **269**, 513 (1995).
- [53] D. Howell, R. P. Behringer, and C. Veje, *Phys. Rev. Lett.* **82**, 5241 (1999).
- [54] E. Andò, S. A. Hall, G. Viggiani, J. Desrues, and P. Bésuelle, *Géotechnique Letters* **2**, 107 (2012).
- [55] O. Gendelman, Y. G. Pollack, I. Procaccia, S. Sengupta, and J. Zylberg, *Phys. Rev. Lett.* **116**, 078001 (2016); [arXiv:1505.06626](https://arxiv.org/abs/1505.06626).
- [56] E. Berthier, M. A. Porter, and K. E. Daniels, *Proc. Natl. Acad. Sci. USA* **116**, 16742 (2019).
- [57] A. Tordesillas, *Philos. Mag.* **87**, 4987 (2007).
- [58] N. Guo and J. Zhao, *Comput. Geotechnics* **47**, 1 (2013).
- [59] M. R. Kuhn, *Mech. Mater.* **31**, 407 (1999).
- [60] M. Pouragha and R. Wan, *Int. J. Solids Struct.* **110**, 94 (2017).
- [61] S. Edwards and R. Oakeshott, *Physica A* **157**, 1080 (1989).
- [62] R. Blumenfeld and S. F. Edwards, *J. Phys. Chem. B* **113**, 3981 (2009).
- [63] R. Blumenfeld, J. F. Jordan, and S. F. Edwards, *Phys. Rev. Lett.* **109**, 238001 (2012).
- [64] D. Bi, S. Henkes, K. E. Daniels, and B. Chakraborty, *Annu. Rev. Condens. Matter Phys.* **6**, 63 (2015).
- [65] A. Baule, F. Morone, H. J. Herrmann, and H. A. Makse, *Rev. Mod. Phys.* **90**, 015006 (2018).
- [66] E. S. Bililign, J. E. Kollmer, and K. E. Daniels, *Phys. Rev. Lett.* **122**, 038001 (2019).
- [67] P. Ball, *Nat. Mater.* **18**, 196 (2019).
- [68] S. Masson and J. Martinez, *J. Eng. Mech.* **127**, 1007 (2001).
- [69] J. Desrues and G. Viggiani, *Inte. J. Numer. Analytical Methods Geomechanics* **28**, 279 (2004).
- [70] J. Desrues and W. Hammad, in *Proceedings of the International Workshop on Numerical Methods for Localization and Bifurcation of Granular Bodies* (Technical University of Gdańsk, Gdańsk, 1989), pp. 57–67.
- [71] M. Pouragha and R. Wan, *J. Eng. Mech.* **143**, C4016002 (2017).
- [72] I. C. G. Inc, computer code PFC2D, Itasca Consulting Group Inc., Minneapolis, MN, 2008, <http://docs.itascacg.com/pfc600/pfc/docproject/>.
- [73] F. da Cruz, S. Emam, M. Prochnow, J.-N. Roux, and F. Chevoir, *Phys. Rev. E* **72**, 021309 (2005).
- [74] F. Radjai and S. Roux, *Phys. Rev. Lett.* **89**, 064302 (2002).
- [75] S. Bonfanti, R. Guerra, C. Mondal, I. Procaccia, and S. Zapperi, *Phys. Rev. E* **100**, 060602(R) (2019).
- [76] F. Nicot, H. Xiong, A. Wautier, J. Lerbet, and F. Darve, *Granular Matter* **19**, 18 (2017).
- [77] M. Pouragha and R. Wan, *Mech. Mater.* **126**, 57 (2018).
- [78] A. Lemaître and C. Caroli, *Phys. Rev. Lett.* **103**, 065501 (2009).
- [79] K. LU, E. E. Brodsky, and H. P. Kavehpour, *J. Fluid Mech.* **587**, 347 (2007).
- [80] F. Nicot, N. Hadda, F. Bourrier, L. Sibille, R. Wan, and F. Darve, *Int. J. Solids Struct.* **49**, 1252 (2012).
- [81] R. Maimon and J. M. Schwarz, *Phys. Rev. Lett.* **92**, 255502 (2004).
- [82] V. Privman, *Finite Size Scaling and Numerical Simulation of Statistical Systems* (World Scientific, Singapore, 1990).
- [83] See Supplemental Material at <http://link.aps.org/supplemental/10.1103/PhysRevE.104.024901> for additional figures.
- [84] C. Liu, E. E. Ferrero, F. Puosi, J.-L. Barrat, and K. Martens, *Phys. Rev. Lett.* **116**, 065501 (2016).
- [85] S. Zapperi, A. Vespignani, and H. E. Stanley, *Nature (London)* **388**, 658 (1997).

- [86] J. Baró and E. Vives, *Phys. Rev. E* **85**, 066121 (2012).
- [87] K. Christensen, N. Farid, G. Pruessner, and M. Stapleton, *Eur. Phys. J. B* **62**, 331 (2008).
- [88] K. Karimi and J.-L. Barrat, *Phys. Rev. E* **93**, 022904 (2016).
- [89] D. Amitrano, *J. Geophys. Res.* **108**, 2109 (2003).
- [90] C. Lord-May, J. Baró, D. W. Eaton, and J. Davidsen, *Phys. Rev. Research* **2**, 043324 (2020).
- [91] Didier Sornette, *J. Phys. I France* **4**, 209 (1994).
- [92] F. Vazquez, J. A. Bonachela, C. López, and M. A. Muñoz, *Phys. Rev. Lett.* **106**, 235702 (2011).
- [93] T. Utsu, Y. Ogata, Ritsuko S, and Matsu'ura, *J. Phys. Earth* **43**, 1 (1995).
- [94] J. Weiss and M. Carmen Miguel, *Mater. Sci. Eng. A* **387–389**, 292 (2004).
- [95] R. Crane and D. Sornette, *Proc. Natl. Acad. Sci. USA* **105**, 15649 (2008).
- [96] D. Sornette and S. Utkin, *Phys. Rev. E* **79**, 061110 (2009).
- [97] J. Baró, A. Corral, X. Illa, A. Planes, E. K. H. Salje, W. Schranz, D. E. Soto-Parra, and E. Vives, *Phys. Rev. Lett.* **110**, 088702 (2013).
- [98] S. Hainzl, J. Moradpour, and J. Davidsen, *Geophys. Res. Lett.* **41**, 8818 (2014).
- [99] J. Baró, J.-M. Martín-Olalla, F. J. Romero, M. C. Gallardo, E. K. H. Salje, E. Vives, and A. Planes, *J. Phys.: Condens. Matter* **26**, 125401 (2014).
- [100] J. Davidsen, G. Kwiatek, E.-M. Charalampidou, T. Goebel, S. Stanchits, M. Rück, and G. Dresen, *Phys. Rev. Lett.* **119**, 068501 (2017).
- [101] P. Kumar, E. Korkolis, R. Benzi, D. Denisov, A. Niemeijer, P. Schall, F. Toschi, and J. Trampert, *Sci. Rep.* **10**, 626 (2020).
- [102] J. H. Dieterich, *J. Geophys. Res. (1896-1977)* **77**, 3771 (1972).
- [103] S. Hainzl, G. Zöller, and J. Kurths, *J. Geophys. Res.: Solid Earth* **104**, 7243 (1999).
- [104] G. Zöller, S. Hainzl, Y. Ben-Zion, and M. Holschneider, *Tectonophysics* **423**, 137 (2006).
- [105] Y. Ben-Zion and V. Lyakhovsky, *Geophys. J. Int.* **165**, 197 (2006).
- [106] E. A. Jagla, *Phys. Rev. E* **90**, 042129 (2014).
- [107] X. Zhang and R. Shcherbakov, *Sci. Rep.* **6**, 36668 EP (2016), article.
- [108] J. Baró and J. Davidsen, *Phys. Rev. E* **97**, 033002 (2018).
- [109] C. Ruscher and J. Rottler, *Soft Matter* **16**, 8940 (2020).
- [110] S. Touati, M. Naylor, and I. G. Main, *Phys. Rev. Lett.* **102**, 168501 (2009).
- [111] J. Baró and J. Davidsen, *European Phys. J.: Special Topics* **226**, 3211 (2017).
- [112] M. R. Kuhn and A. Daouadji, *Granular Matter* **21**, 10 (2019).
- [113] H. Bi, G. Börner, and Y. Chu, *Astron. Astrophys.* **218**, 19 (1989).
- [114] H. F. Reid, The California Earthquake of April 18, 1906, Report of the State Earthquake Investigation Commission, The Bancroft Library, University of California, Berkeley, CA, USA, 1910.
- [115] K. Shimazaki and T. Nakata, *Geophys. Res. Lett.* **7**, 279 (1980).
- [116] G. Combe and J.-N. Roux, *Phys. Rev. Lett.* **85**, 3628 (2000).
- [117] G. Picard, A. Ajdari, F. Lequeux, and L. Bocquet, *European Phys. J. E* **15**, 371 (2004).
- [118] T. Albaret, A. Tanguy, F. Boioli, and D. Rodney, *Phys. Rev. E* **93**, 053002 (2016).
- [119] D. Lockner, *Inte. J. Rock Mech. Mining Sci Geomech. Abstr.* **30**, 883 (1993).
- [120] S. Lennartz-Sassinek, I. G. Main, M. Zaiser, and C. C. Graham, *Phys. Rev. E* **90**, 052401 (2014).
- [121] J. Baró, K. A. Dahmen, J. Davidsen, A. Planes, P. O. Castillo, G. F. Nataf, E. K. H. Salje, and E. Vives, *Phys. Rev. Lett.* **120**, 245501 (2018).
- [122] F. Kun, I. Varga, S. Lennartz-Sassinek, and I. G. Main, *Phys. Rev. Lett.* **112**, 065501 (2014).
- [123] G. Kwiatek, T. H. W. Goebel, and G. Dresen, *Geophys. Res. Lett.* **41**, 5838 (2014).
- [124] A. Tordesillas, J. Zhang, and R. Behringer, *Geomech. Geoengineer.: Int. J.* **4**, 3 (2009).
- [125] C.-C. Vu and J. Weiss, *Phys. Rev. Lett.* **125**, 105502 (2020).
- [126] S. Janičević, L. Laurson, K. J. Måløy, S. Santucci, and M. J. Alava, *Phys. Rev. Lett.* **117**, 230601 (2016).
- [127] L. Salditch, S. Stein, J. Neely, B. D. Spencer, E. M. Brooks, A. Agnon, and M. Liu, *Tectonophysics* **774**, 228289 (2020).
- [128] K. Karimi, E. E. Ferrero, and J.-L. Barrat, *Phys. Rev. E* **95**, 013003 (2017).
- [129] J. L. Anthony and C. Marone, *J. Geophys. Res.* **110** (2005), doi: 10.1029/2004JB003399.
- [130] G. Frenkel, R. Blumenfeld, Z. Grof, and P. R. King, *Phys. Rev. E* **77**, 041304 (2008).
- [131] S. Henkes, C. S. O'Hern, and B. Chakraborty, *Phys. Rev. Lett.* **99**, 038002 (2007).
- [132] E. A. Jagla, *Phys. Rev. E* **92**, 042135 (2015).
- [133] J. Barés, D. Wang, D. Wang, T. Bertrand, C. S. O'Hern, and R. P. Behringer, *Phys. Rev. E* **96**, 052902 (2017).
- [134] Y. T. Feng and W. Gao, *Powder Tech.* **389**, 376 (2021).
- [135] A. H. Clark, A. J. Petersen, L. Kondic, and R. P. Behringer, *Phys. Rev. Lett.* **114**, 144502 (2015).
- [136] R. Niemann, J. Baró, O. Heczko, L. Schultz, S. Fähler, E. Vives, L. Mañosa, and A. Planes, *Phys. Rev. B* **86**, 214101 (2012).
- [137] C. S. Chang, S. J. Chao, and Y. Chang, *Int. J. Solids Struct.* **32**, 1989 (1995).
- [138] M. Pouragha and R. Wan, *Int. J. Solids Struct.* **138**, 97 (2018).